

# On the population III binary black hole mergers with intermediate mass black holes: dependence on common envelope parameter

Kotaro Hijikawa,<sup>1\*</sup> Tomoya Kinugawa,<sup>2</sup> Ataru Tanikawa,<sup>3</sup> Takashi Yoshida<sup>4,1</sup> and Hideyuki Umeda<sup>1</sup>

<sup>1</sup>*Department of Astronomy, Graduate School of Science, The University of Tokyo, 7-3-1 Hongo, Bunkyo-ku, 113-0033 Tokyo, Japan*

<sup>2</sup>*Institute for Cosmic Ray Research, The University of Tokyo, Kashiwa, Chiba, Japan*

<sup>3</sup>*Department of Earth Science and Astronomy, College of Arts and Sciences, The University of Tokyo, Meguro-ku, Tokyo, Japan*

<sup>4</sup>*Yukawa Institute for Theoretical Physics, Kyoto University, Kitashirakawa Oiwakecho, Sakyo-ku, Kyoto 606-8502, Japan*

Accepted XXX. Received YYY; in original form ZZZ

## ABSTRACT

The current gravitational wave (GW) detectors have successfully observed many binary compact objects, and the third generation ground-based GW detectors such as Einstein telescope and space-borne detectors such as LISA will start their GW observation in a decade. Ahead of the arrival of this new era, we perform a binary population synthesis calculation for very massive ( $\sim 100\text{--}1000 M_{\odot}$ ) population (Pop.) III stars, derive the various property of binary black hole (BBH) mergers with intermediate mass black holes (IMBHs) and investigate the dependence on common envelope parameter  $\alpha\lambda$  which is still not a well understood parameter. We find that the maximum mass of primary BH mass is larger for smaller value of common envelope parameter. In this study, we adopt double power law initial mass function (IMF) for Pop. III stars, and put some constraints on Pop. III IMF by comparing our obtained merger rate density at the local Universe with that derived from gravitational wave (GW) observation. We compute the detection rate and show that the third generation ground-based GW detector, Einstein telescope, have a potential to detect  $\sim 10\text{--}1000$  BBHs with IMBHs per year. We also find that we may be able to obtain the insight into  $\alpha\lambda$  if a BBH with total mass  $\gtrsim 500M_{\odot}$  are detected by advanced LIGO (O4) or LISA.

**Key words:** stars: Population III, binaries: general, black hole mergers, gravitational waves

## 1 INTRODUCTION

Many binary black hole (BBH) mergers have been discovered by the gravitational wave (GW) detectors, advanced LIGO and Virgo. The catalog, GWTC-3, was released last year by the LIGO Scientific Collaboration, the Virgo Collaboration and the KAGRA Collaboration (The LIGO Scientific Collaboration et al. 2021b), and the number of discovered BBH mergers is approaching 100. Detected BBHs have relatively high mass ( $\sim 20\text{--}50 M_{\odot}$ ) compared to Galactic BHs, and have low spin ( $\sim 0$ ). Origin of such discovered BBH mergers have been suggested by many authors. For example, field population (Pop.) I or II isolated binary stars (e.g., Bethe & Brown 1998; Marchant et al. 2016; Mandel & de Mink 2016; Stevenson et al. 2017; Eldridge et al. 2017, 2019; Mapelli et al. 2017, 2019, 2021; Kruckow et al. 2018; Belczynski et al. 2020; Bavera et al. 2021; Riley et al. 2021), Pop. III isolated binary stars (e.g., Kinugawa et al. 2014, 2016, 2020, 2021b; Hartwig et al. 2016; Belczynski et al. 2017; Tanikawa et al. 2021b, 2022), a dynamical formation in stellar clusters (e.g. Portegies Zwart & McMillan 2000; O’Leary et al. 2006; Sadowski et al. 2008; Banerjee et al. 2010; Banerjee 2017, 2018a,b, 2021a,b; Downing et al. 2010, 2011; Tanikawa 2013; Bae et al. 2014; Ziosi et al. 2014; Mapelli 2016; Rodriguez et al. 2016, 2018, 2019; Fujii et al. 2017; Park et al. 2017; Hong et al. 2018, 2020; Samsing 2018; Samsing et al. 2018; Di Carlo et al. 2019, 2020; Kumamoto et al. 2019, 2020, 2021; Anagnostou et al. 2020; Kremer et al. 2020; Fragione &

Banerjee 2021; Trani et al. 2021; Weatherford et al. 2021), a Pop. III dynamical formation (e.g. Liu & Bromm 2020, 2021; Liu et al. 2021; Wang et al. 2022), a formation in the galactic nuclei (e.g. O’Leary et al. 2009; Antonini & Perets 2012; Antonini & Rasio 2016; Stone et al. 2017; Leigh et al. 2018; McKernan et al. 2018; Rasskazov & Kocsis 2019; Yang et al. 2019; Arca Sedda 2020; Tagawa et al. 2020a,b, 2021a,b), or triple or multiple star systems (e.g. Antonini et al. 2017; Silsbee & Tremaine 2017; Rodriguez & Antonini 2018; Fragione & Kocsis 2019; Fragione et al. 2020; Hamers et al. 2021; Trani et al. 2022; Vynatheya & Hamers 2022).

In addition to the typical population, a more massive BBH, GW190521, with total mass  $\sim 150M_{\odot}$  is also discovered (Abbott et al. 2020). Since its primary BH mass is about  $90 M_{\odot}$  and it lies in the pair-instability mass gap<sup>1</sup>, it is considered to be difficult to form such BBHs through a general isolated binary formation channel, and the hierarchical merger process in the dynamical formation scenario can explain the existence of  $\sim 90M_{\odot}$  BH. However, there are some isolated binary scenarios to explain the formation of GW190521. For example, by reducing  $^{12}\text{C}(\alpha, \gamma)^{16}\text{O}$  reaction rate within its uncertainty, the pair-instability mass gap shifts toward the heavier side, and GW190521-like BBHs can be formed through isolated binary formation channel (Farmer et al. 2019, 2020; Belczynski 2020). Furthermore, a massive extremely metal-poor star or a Pop. III star may

<sup>1</sup> Note that GW190521 may be a pair of two BHs above and below the pair-instability mass gap (Fishbach & Holz 2020; Nitz & Capano 2021).

\* E-mail: hijikawa@astron.s.u-tokyo.ac.jp

be able to become a BH with 65–100  $M_{\odot}$ , and thus the pair-instability mass gap may be filled, and GW190521-like BBHs can be formed through isolated binary formation channel (Umeda et al. 2020; Kinugawa et al. 2021a; Tanikawa et al. 2021a,b; Farrell et al. 2021; Vink et al. 2021). From the discovery of GW190521 and studies on this observation, the equivalent objects or more massive BBH mergers, i.e., the mergers of an intermediate mass black hole (IMBH;  $\geq 100M_{\odot}$ ) with a stellar mass BH or an IMBH are expected to be detected by the future GW observations.

So far, a number of stellar mass BHs ( $\leq 100M_{\odot}$ ) have been found by GW observations or X-ray binary observations. On the other hand, few IMBHs have yet been discovered (one can find more information about the searches for IMBHs in the review, Greene et al. 2020). The most reliable one is the merger remnant of the BBH merger, GW190521 (Abbott et al. 2020). The X-ray sources HLX-1 is also considered to be an IMBH (Farrell et al. 2009). The presence of the supermassive BHs (SMBHs;  $\geq 10^6 M_{\odot}$ ) at the center of galaxies has been confirmed, and recently the Event Horizon Telescope successfully got images of SMBHs at the center of M87 (Event Horizon Telescope Collaboration et al. 2019a,b,c,d,e,f) and the Milky Way (Event Horizon Telescope Collaboration et al. 2022a,b,c,d,e,f). The formation and evolution of SMBHs are still not well understood. According to some models, the seed of SMBHs has repeatedly merged with other BHs multiple times and increases its mass. Since there are few IMBHs that have been found, it is difficult to constrain the formation theory and to know where the SMBHs came from. Therefore, it is important to know what mass of IMBHs existed at each redshift in order to impose restrictions on the formation model of the SMBH. As well as the probe for SMBH, IMBHs may be useful for other problems. For example, the findings of IMBHs just above the pair-instability mass gap can be used as the “standard siren” for the cosmology (Farr et al. 2019; Farmer et al. 2019, 2020). From the GW observation, the luminosity distance and the redshifted mass can be obtained. If we have a knowledge of the upper end of the pair-instability mass gap, then we can get the redshift of the sources from the true and redshifted mass. Furthermore, the pair of stellar mass BH and IMBH, or the intermediate mass ratio inspiral (also known as IMRI) will allow us to test the gravitational theory (e.g., Sopuerta & Yunes 2009; Amaro-Seoane 2018).

In the future, the third generation ground-based GW detector, Einstein telescope (Punturo et al. 2010; Sathyaprakash et al. 2012) or Cosmic Explorer (Reitze et al. 2019), and space-borne GW detector, LISA (Amaro-Seoane et al. 2017), TianQin (Luo et al. 2016; Wang et al. 2019), TianGO (Kuns et al. 2020), or DECIGO (Seto et al. 2001) will start the construction in ten years. Since their sensitivity will improve and their horizon redshift will be  $z \sim 10\text{--}1000$  for BBH mergers with total mass  $M_t \sim 10\text{--}10\,000 M_{\odot}$ , the inspiral and merger of more massive BBHs, or binary IMBHs, located in the earlier Universe are expected to be discovered. Previously, the GWs from IMBH-IMBH mergers during the runaway merging process were investigated (e.g., Matsubayashi et al. 2004; Shinkai et al. 2017). As to the isolated binary, the BBH mergers above the pair-instability mass gap originated from isolated Pop. III binaries were investigated by Mangiagli et al. (2019). Pop. III star formation simulations have been performed (e.g., Hirano et al. 2014, 2015; Susa et al. 2014), and it is claimed that the typical Pop. III stellar mass is 10–100  $M_{\odot}$ . Furthermore, very massive ( $\sim 100\text{--}1000 M_{\odot}$ ) Pop. III stars might be formed (e.g., Hirano et al. 2015). A Pop. III star with 100–200  $M_{\odot}$  finally causes the pair-instability supernova, and leaves no remnant. On the other hand, more massive Pop. III star than this directly collapses and finally becomes an IMBH. Therefore, in our previous paper (Hijikawa et al. 2021), we focused on the

very massive ( $\sim 100\text{--}1000 M_{\odot}$ ) Pop. III stars, performed binary population synthesis calculation, derived the merger rate density of BBHs with IMBHs assuming single power law initial mass function (IMF), and compared this with the observation. Thus far, no BBH with IMBHs have been discovered, and hence the upper limit on the merger rate density is obtained. We compared our results with this upper limit, and found that the power of single power law IMF needs to be lower than 2.8. However, this is inconsistent with the results of Pop. III star formation simulation claiming a relatively top heavy IMF where  $\leq 100M_{\odot}$ .

In this study, we adopt the double power law IMF with extensive parameter range, perform a binary population synthesis calculation, and investigate what types of BBH mergers with IMBHs will be observed by current and future GW detectors when using a reasonable IMF which meets the Pop. III star formation simulation and current GW observation. In addition, we investigate the dependence of the properties of BBHs with IMBHs on the common envelope parameter  $\alpha\lambda$ .

This paper is constructed as follows. In Section 2, we describe our method of binary population synthesis calculations. In Section 3, we show the formation channel, primary BH mass distribution, mass ratio distribution, effective spin distribution, delay time distribution and the redshift evolution of merger rate density for all sub-populations of BBH mergers with IMBHs. We also show in detail the dependence of such distribution on the common envelope parameter  $\alpha\lambda$ . We compare our obtained merger rate density with the upper limit and impose restrictions on IMF and  $\alpha\lambda$  models, and compute the detection rate and detected BBH mass distribution in Section 4. Finally, we summarize our paper in Section 5.

## 2 METHOD

In order to calculate the merger rate density of Pop. III BBH mergers for various Pop. III IMFs, we perform binary population synthesis calculations. Our binary population synthesis code is identical with that of Hijikawa et al. (2021). In section 2.1, we overview the stellar and binary evolution implemented in our code. In section 2.2, we describe IMFs and other initial conditions we adopt. How we compute the merger rate density of Pop. III BBH mergers is described in Section 2.3. Finally, in Section 2.4, we summarize our parameter sets.

### 2.1 Stellar and Binary Evolution Physics

Our binary population synthesis code is based on BSE (Hurley et al. 2000, 2002)<sup>1</sup>. Some additions and changes have been made to this, and these are described below.

In our code, the fitting formulae for  $Z = 10^{-8}Z_{\odot}$  stars were implemented (Tanikawa et al. 2020, 2021a,b, 2022), published as BSEEMP<sup>2</sup>.  $Z$  and  $Z_{\odot} = 0.02$  are the stellar metallicity and solar metallicity, respectively. In their studies, the evolution of  $Z = 10^{-8}Z_{\odot}$  stars up to 1280  $M_{\odot}$  are calculated by the 1D stellar evolution code, HOSHI (Takahashi et al. 2016, 2019, 2018; Yoshida et al. 2019). In our study, we treat  $Z = 10^{-8}Z_{\odot}$  stars as Pop. III stars ( $Z = 0$ ). There is little difference in the stellar evolution between  $Z = 10^{-8}Z_{\odot}$  stars and  $Z = 0$  stars for the following reason. As the abundance of heavy elements in a  $Z = 10^{-8}Z_{\odot}$  star is extremely low, the CNO cycle

<sup>1</sup> <http://astronomy.swin.edu.au/~jhurley/>

<sup>2</sup> <https://github.com/atrnkw/bseemp>

does not operate initially. The abundance of carbon, nitrogen and oxygen are increased by the triple alpha reaction, and then the CNO cycle commences. These evolutionary properties are same as those of  $Z = 0$  stars. Therefore, the difference in metallicity,  $Z = 10^{-8}Z_{\odot}$  and  $Z = 0$ , has little effect on the stellar evolution. Our code has two stellar models in which the convective overshooting is more effective and less so, L and M models (Yoshida et al. 2019; Tanikawa et al. 2020, 2021a,b, 2022). In this paper, we use only L model.

We adopt the ‘rapid’ model in Fryer et al. (2012) with the modification for the pulsational pair-instability and pair-instability supernova (see equations 5–7 in Tanikawa et al. 2021b). We assume that the mass of a BH formed through pulsational pair-instability is  $45 M_{\odot}$ , and the minimum helium core mass of direct collapse is  $135 M_{\odot}$  in the same way as Belczynski et al. (2016). Therefore, the mass range of pair-instability mass gap is 45–135  $M_{\odot}$ .

In a binary system, orbital angular momenta and spin angular momenta are exchanged by tidal interaction. In our code, the tidal coefficient factor  $E$  for the dynamical tide is implemented as

$$E = \begin{cases} 10^{-0.42} \left( \frac{R_{\text{con}}}{R} \right)^{7.5} & \text{for H-rich stars,} \\ 10^{-0.93} \left( \frac{R_{\text{con}}}{R} \right)^{6.7} & \text{for He-rich stars,} \end{cases} \quad (1)$$

(Qin et al. 2018), where  $R$  is the stellar radius and  $R_{\text{con}}$  is the convective core radius, respectively. We use the values  $R_{\text{con}} = 1R_{\odot}$  and  $0.5R_{\odot}$  for main-sequence stars and naked helium stars, respectively (Tanikawa et al. 2020; Kinugawa et al. 2020).

When one of the star in the binary system fills its Roche lobe, the stellar mass overflows. If this mass transfer is unstable, the binary system enters a common envelope phase; if not, the stable mass transfer occurs. In our code, the mass transfer rate of stable mass transfer is calculated as

$$\dot{M}_{\text{don}} = - \frac{f(\mu)M_{\text{don}}}{\sqrt{R_{\text{don}}^3/GM_{\text{don}}}} \left( \frac{\Delta R_{\text{don}}}{R_{\text{don}}} \right)^{n+3/2} dn, \quad (2)$$

where

$$f(\mu) = \frac{4\mu\sqrt{\mu}\sqrt{1-\mu}}{(\sqrt{\mu} + \sqrt{1-\mu})^4} \left( \frac{a}{R_{\text{don}}} \right)^3, \quad (3)$$

$\mu = M_{\text{don}}/M_{\text{tot}}$ ,  $\Delta R_{\text{don}} = R_{\text{don}} - R_{\text{L, don}}$ ,  $G$ ,  $M_{\text{don}}$ ,  $R_{\text{don}}$ ,  $n$ ,  $dn$ ,  $a$ ,  $M_{\text{tot}}$ , and  $R_{\text{L, don}}$  are the gravitational constant, the donor mass, the donor radius, the polytropic index of the donor star, the normalization factor depending on  $n$ , orbital separation, the total mass, and the donor Roche lobe radius, respectively (e.g., Paczyński & Sienkiewicz 1972; Savonije 1978; Edwards & Pringle 1987). In our study, we assume that the mass transfer is conservative, unless the accretor is a compact object.

If a mass transfer becomes unstable ( $\zeta_{\text{L}} > \zeta_{\text{ad}}$ ), the binary system enters a common envelope phase.  $\zeta_{\text{L}} = d \log R_{\text{L}} / d \log M$  is the response of the Roche lobe radius  $R_{\text{L}}$  to the change in stellar mass  $M$  and  $\zeta_{\text{ad}} = (d \log R / d \log M)_{\text{ad}}$  is the response of stellar radius  $R$  to the change in stellar mass within the dynamical timescale. We use the same  $\zeta_{\text{ad}}$  value as Kinugawa et al. (2014), and this criteria is roughly consistent with Pavlovskii et al. (2017). In this study, we use the  $\alpha\lambda$  formalism for common envelope evolution (Webbink 1984), and the orbital separation just after the common envelope phase  $a_{\text{f}}$  is calculated by the following energy budget if the accretor star does not have a clear core-envelope structure.

$$\alpha \left( \frac{GM_{\text{c, don}}M_{\text{acc}}}{2a_{\text{f}}} - \frac{GM_{\text{don}}M_{\text{acc}}}{2a_{\text{i}}} \right) = \frac{GM_{\text{don}}M_{\text{env, don}}}{\lambda R_{\text{don}}}. \quad (4)$$

Here,  $M_{\text{c, don}}$  and  $M_{\text{env, don}}$  are the stellar core and envelope mass of the donor star,  $M_{\text{acc}}$  is the accretor stellar mass and  $a_{\text{i}}$  is the orbital separation just before the common envelope phase.  $\alpha$  is the efficiency parameter showing how much orbital energy is used to strip the stellar envelope.  $\lambda$  is the binding energy parameter. The value of the common envelope parameters,  $\alpha$  and  $\lambda$ , are still not well known. Thus, in this study, we use various values for the product of the common envelope parameters,  $\alpha\lambda$ :  $\alpha\lambda = 0.01, 0.1, 0.5, 1.0, 2.0$  and  $5.0$ . We call the common envelope phase during which the accretor star does not have a core-envelope structure ‘‘single common envelope’’.

When the accretor star which does not fill its Roche lobe is also a giant star, the orbital energy is used to strip the envelope of both stars. We call this common envelope ‘‘double common envelope’’, and the orbital separation just after the common envelope phase  $a_{\text{f}}$  is calculated as

$$\alpha \left( \frac{GM_{\text{c, don}}M_{\text{c, acc}}}{2a_{\text{f}}} - \frac{GM_{\text{don}}M_{\text{acc}}}{2a_{\text{i}}} \right) = \frac{GM_{\text{don}}M_{\text{env, don}}}{\lambda R_{\text{don}}} + \frac{GM_{\text{acc}}M_{\text{env, acc}}}{\lambda R_{\text{acc}}}. \quad (5)$$

$M_{\text{c, acc}}$ ,  $M_{\text{env, acc}}$  and  $R_{\text{acc}}$  are the core and envelope mass and stellar radius of accretor star. In our calculation, when both stars fill their Roche lobes, the binary system enters a common envelope phase even though  $\zeta_{\text{L}} > \zeta_{\text{ad}}$  is not met. We call this common envelope ‘‘contact common envelope’’, and the orbital separation just after the common envelope phase  $a_{\text{f}}$  is calculated as equation (5).

## 2.2 Initial Conditions

In this study, we adopt various IMFs and calculate the merger rate density of BBH mergers. In Section 2.2.1, we briefly review the recent Pop. III star formation simulation, and describe our IMFs for Pop. III stars. Other initial conditions such as initial mass ratio function, initial orbital separation function and initial eccentricity function are shown in Section 2.2.2.

### 2.2.1 Initial Mass Functions

Pop. III stars are formed from metal free gas. Star forming clouds are formed in the mini-halo and at the center the gas cloud collapses due to the  $\text{H}_2$  and HD cooling. The cooling efficiency is weaker than in the Pop. I/II case, and hence the Jeans mass of the gas cloud is larger. According to Pop. III star formation simulation (Hirano et al. 2014, 2015; Susa et al. 2014), the ZAMS mass distribution of Pop. III stars is roughly flat for  $\lesssim 100M_{\odot}$  and there is break around at  $\sim 100M_{\odot}$ . In this study, in order to reproduce this structure, we adopt a double power law IMF for the Pop. III single stars and primary stars of Pop. III binaries. Our double power law IMFs  $f(m)$  have three parameters as shown in the following equations.

$$f(m) \propto \begin{cases} m^{-\gamma_1} & (m_{\text{min}} \leq m \leq m_{\text{crit}}), \\ m_{\text{crit}}^{\gamma_2-\gamma_1} \times m^{-\gamma_2} & (m_{\text{crit}} < m \leq m_{\text{max}}), \end{cases} \quad (6)$$

where  $m$  is the stellar mass and  $m_{\text{min}} = 10 M_{\odot}$  and  $m_{\text{max}} = 1500 M_{\odot}$  are the minimum mass and maximum mass in our calculation, respectively. At the critical mass  $m_{\text{crit}}$ , the slope of the IMF changes from  $\gamma_1$  to  $\gamma_2$ . In order to connect the IMF continuously at  $m = m_{\text{crit}}$ , the coefficient  $m_{\text{crit}}^{\gamma_2-\gamma_1}$  is multiplied. According to Pop. III star formation simulations (Susa et al. 2014; Hirano et al. 2014, 2015), we set the critical mass  $m_{\text{crit}}$  to 100, 200 and 300  $M_{\odot}$ . The slope of lower mass region ( $m < m_{\text{crit}}$ ),  $\gamma_1$ , is set to 0 and 1 to reproduce

a top heavy function in the lower mass region. The slope of higher mass region ( $m > m_{\text{crit}}$ ),  $\gamma_2$ , is set to 1.5, 2.0, 2.5, 3.0, 3.5, 4.0, 4.5 and 5.0.

### 2.2.2 Other Initial Conditions

In order to determine the initial condition, we set the initial mass ratio, initial orbital separation, and initial eccentricity distribution in addition to the IMF. The initial mass ratio distribution is flat ( $\propto \text{const.}$ ), and the mass ratio range is  $q_{\text{min}}^{-1}$ , where  $q_{\text{min}} = 10/M_1$  and  $M_1$  is the mass of initially heavier star. The initial orbital separation distribution is logarithmically flat distribution, and the orbital separation range is  $a_{\text{min}} - 10^5 R_\odot$ , where  $a_{\text{min}}$  is determined so that the ZAMS radius does not exceed the Roche lobe radius. In this study, we assume that the initial eccentricity is zero (circular orbit).

### 2.3 Rate Calculation

In this study, we sample  $N_{\text{sam}} = 10^6$  binaries consisting of ZAMS stars with the metallicity  $10^{-8} Z_\odot$  and primary mass  $\in [10, 1500] M_\odot$  according to various initial functions and follow the evolution of  $N_{\text{sam}}$  binaries for each parameter sets. The detail of parameter sets are described in Section 2.4. The merger rate  $\mathcal{R}(z)$  at the redshift  $z$  is calculated as follows.

$$\mathcal{R}(z(t)) = \int_0^t f_b \frac{\text{SFR}(\tau) n(t-\tau)}{\langle m \rangle N_{\text{sam}}} d\tau. \quad (7)$$

$t$  is the age of the Universe at the redshift  $z$  and is calculated assuming the  $\Lambda$ -CDM cosmology. The Hubble constant is  $H_0 = 67.4 \text{ km s}^{-1} \text{ Mpc}^{-1}$  and the matter density parameter is  $\Omega_{\text{m}0} = 0.315$  (Planck Collaboration et al. 2020). SFR( $\tau$ ) is the star formation rate, and we adopt the star formation history in de Souza et al. (2011) for Pop. III stars, but reduce it by a factor of three (Inayoshi et al. 2016; Kinugawa et al. 2020). We assume that the binary fraction  $f_b$  is 0.5.

$$\langle m \rangle = \int_I m f(m) dm + f_b \int_I dm f(m) \int_{J(m)} m q g(q; m) dq, \quad (8)$$

is the mean mass of Pop. III stellar objects (single stars and binaries).  $q \in (0, 1]$  is the mass ratio,  $I = [m_{\text{min}}, m_{\text{max}}] = [10, 1500] M_\odot$  is the primary mass range,  $g(q; m) = 1/(1 - m_{\text{min}}/m)$  is the initial mass ratio function when the primary mass is  $m$  and  $J(m) = [m_{\text{min}}/m, 1]$  is the initial mass ratio range.

$$n(t) = \frac{\text{the number of BBHs whose delay time is in } [t, t + \delta t]}{\delta t}, \quad (9)$$

is the delay time distribution function and we set  $\delta t = 0.1 \text{ Gyr}$ . As long as we use such a small value for  $\delta t$ , the results do not change.

For all parameter sets, we additionally sample the  $N_{\text{sam}, J} = 10^6$  binaries in the primary initial mass range  $J = [150, 600] M_\odot \subset I$  in order to increase the number of samples efficiently and to obtain the more precise results. In such a case, the merger rate density  $\mathcal{R}(z)$  is calculated as follows.

$$\mathcal{R}(z(t)) = \int_0^t f_b \frac{\text{SFR}(\tau)}{\langle m \rangle} \left( A_J \frac{n_I^{(J)}(t-\tau) + n_J(t-\tau)}{N_{\text{sam}, J}^{(J)} + N_{\text{sam}, J}} + (1 - A_J) \frac{n_I(t-\tau) - n_I^{(J)}(t-\tau)}{N_{\text{sam}, I} - N_{\text{sam}, I}^{(J)}} \right) d\tau, \quad (10)$$

$N_{\text{sam}, I} = N_{\text{sam}}$  is the number of samples for the sampling in the primary initial mass range  $I$ .  $N_{\text{sam}, I}^{(J)} < N_{\text{sam}, I}$  is the number of samples whose primary initial mass is in the range  $J \subset I$  for the

**Table 1.** Parameter sets

Parameter	Value
common envelope parameter, $\alpha\lambda$	0.01, 0.1, 0.5, 1.0, 2.0, 5.0
the slope of the lower mass region, $\gamma_1$	0.0, 1.0
the slope of the higher mass region, $\gamma_2$	1.5, 2.0, 2.5, ..., 4.5, 5.0
critical mass, $m_{\text{crit}}$	100, 200, 300 $M_\odot$

sampling in the primary initial mass range  $I$ .  $n_I(t) = n(t)$  and  $n_J(t)$  are the delay time distribution for the sampling in the primary initial mass range  $I$  and  $J$ , respectively.  $n_I^{(J)}(t) < n_I(t)$  is the delay time distribution of BBHs whose primary initial mass is in the range  $J$  for the sampling in the primary initial mass range  $I$ . Finally,

$$A_J = \int_J f(m) dm < \int_I f(m) dm = 1, \quad (11)$$

is calculated from an IMF.

### 2.4 Parameter Sets

As written in Section 2.1 and Section 2.2.1, we use  $\alpha\lambda = 0.01, 0.1, 0.5, 1.0, 2.0$  and  $5.0$  for common envelope evolution, and  $\gamma_1 = 0.0, 1.0, \gamma_2 = 1.5, 2.0, 2.5, 3.0, 3.5, 4.0, 4.5$  and  $5.0$ , and  $m_{\text{crit}}/M_\odot = 100, 200$  and  $300$  for the Pop. III IMF. Therefore, the number of IMFs in our study is  $2 \times 8 \times 3 = 48$ , and thus the number of parameter sets in our study is  $6 \times 48 = 288$ . For these sets, we perform the binary population synthesis calculation and compute the merger rate density of Pop. III BBH mergers. Finally, we summarize our parameter sets in Table 1.

## 3 RESULTS

The BHs in the mass range  $45\text{--}135 M_\odot$  cannot be formed due to the pair-instability effect (see Section 2.1). Therefore, the BBHs with IMBHs ( $> 100 M_\odot$ ) are classified into two types. In this paper, we call a BH whose mass is lower than the lower edge of pair-instability mass gap ( $45 M_\odot$ ) ‘‘low mass BH’’ and call a BH whose mass is higher than the upper edge of pair-instability mass gap ( $135 M_\odot$ ) ‘‘high mass BH’’. We describe the pair of ‘‘low mass BH’’ and ‘‘high mass BH’’ as ‘‘low mass + high mass’’ and describe the pair of ‘‘high mass BH’’s as ‘‘high mass + high mass’’. In Section 3.1 and 3.2, we show the primary BH mass, mass ratio, effective spin, delay time and merger rate density of ‘‘high mass + high mass’’ and ‘‘low mass + high mass’’. We also discuss the dependence of these distribution on common envelope parameter  $\alpha\lambda$ .

### 3.1 ‘‘high mass + high mass’’

#### 3.1.1 formation channel

First, we introduce the dominant formation channel of ‘‘high mass + high mass’’ for each common envelope parameter  $\alpha\lambda$ . In our calculation, when  $\alpha\lambda = 0.5, 1.0, 2.0$  and  $5.0$ , ‘‘high mass + high mass’’ BBHs are formed through ‘‘double common envelope channel’’ and ‘‘contact common envelope channel’’. The definitions of these evolutionary channels are that a binary system pass through one ‘‘double common envelope’’ and ‘‘contact common envelope’’, respectively (see Section 2.1). An example of ‘‘double common envelope channel’’ and ‘‘contact common envelope channel’’ are shown in Figure



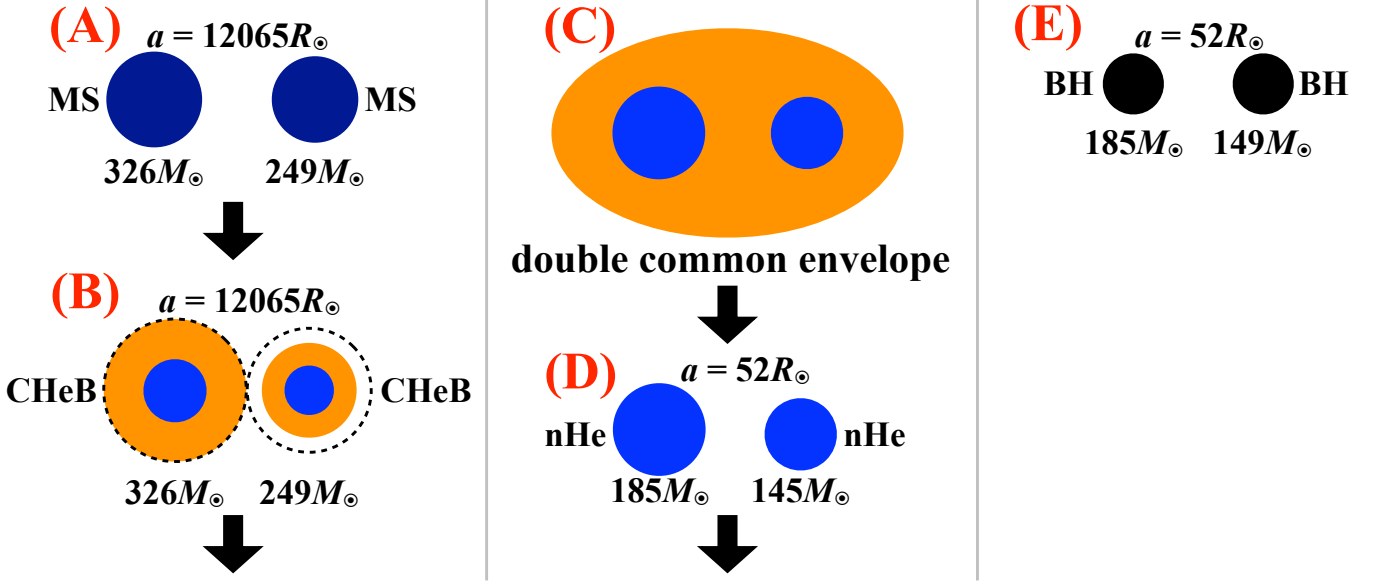


**Figure 1.** An example of “double common envelope channel” when  $\alpha\lambda = 1.0$ . “CHeB” and “nHe” stand for the core helium burning phase and naked helium star, respectively. The dashed circles in phase (B) indicate the Roche lobes of both stars.

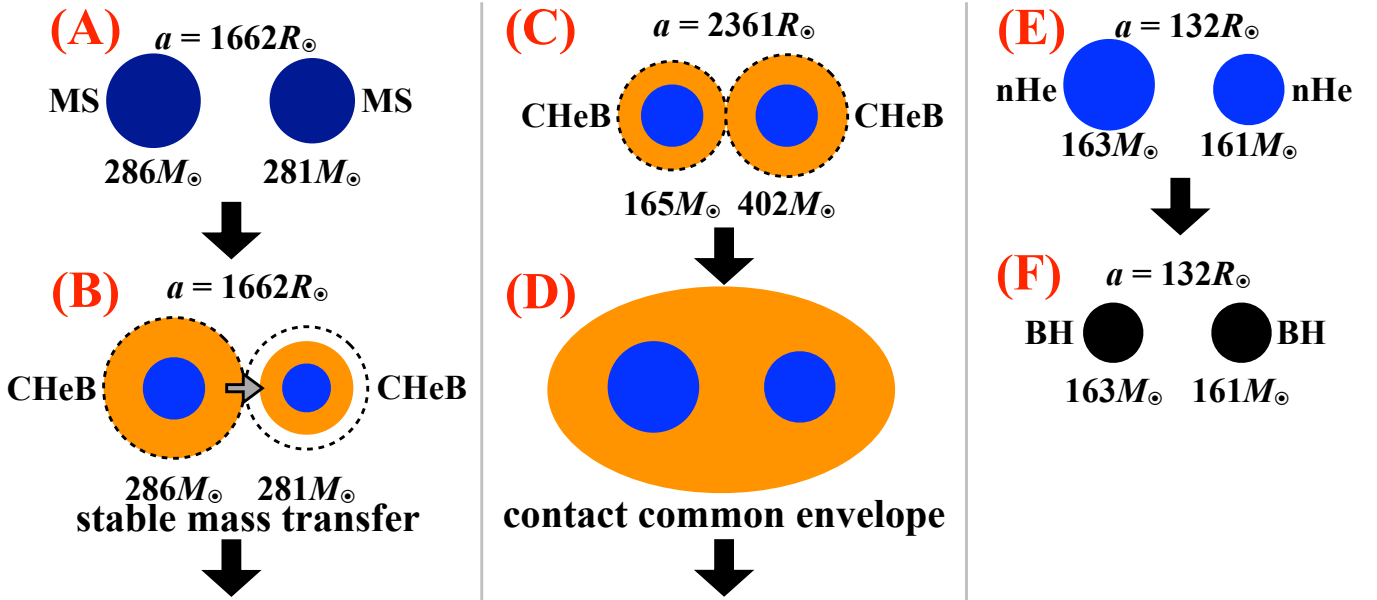


**Figure 2.** An example of “contact common envelope channel” when  $\alpha\lambda = 1.0$ .

1 and 2 (for  $\alpha\lambda = 1.0$ ). When  $\alpha\lambda = 0.1$ , “single common envelope channel (2)” emerges and becomes dominant in addition to “double common envelope channel” and “contact common envelope channel”. “Single common envelope channel (2)” is the evolutionary channel that passes through one “single common envelope” whose donor star is the secondary star at the ZAMS time, i.e., the initially lighter star. When  $\alpha\lambda = 0.01$ , only “single common envelope channel (2)” can form a merging BBH. An example channel is shown in Figure 3 (for  $\alpha\lambda = 0.01$ ). Almost all BBH formed through “single common envelope channel (2)” are mass inverted.

In general, it is easier to shrink through “double common envelope channel” and “contact common envelope channel” than through

“single common envelope channel (2)” because more orbital energy are used to strip the stellar envelope through the former common envelope than the latter common envelope. Therefore, if  $\alpha\lambda$  is too small such as 0.01, the binary system entering “double common envelope channel” and “contact common envelope channel” coalesces after the common envelope phase, and thus they cannot form a merging BBH. On the other hand, when  $\alpha\lambda = 0.5, 1.0, 2.0$ , it is impossible to shrink the orbital separation sufficiently to merge within a Hubble time through “single common envelope channel (2)”. When  $\alpha\lambda = 0.1$ , both formation channels can occur.

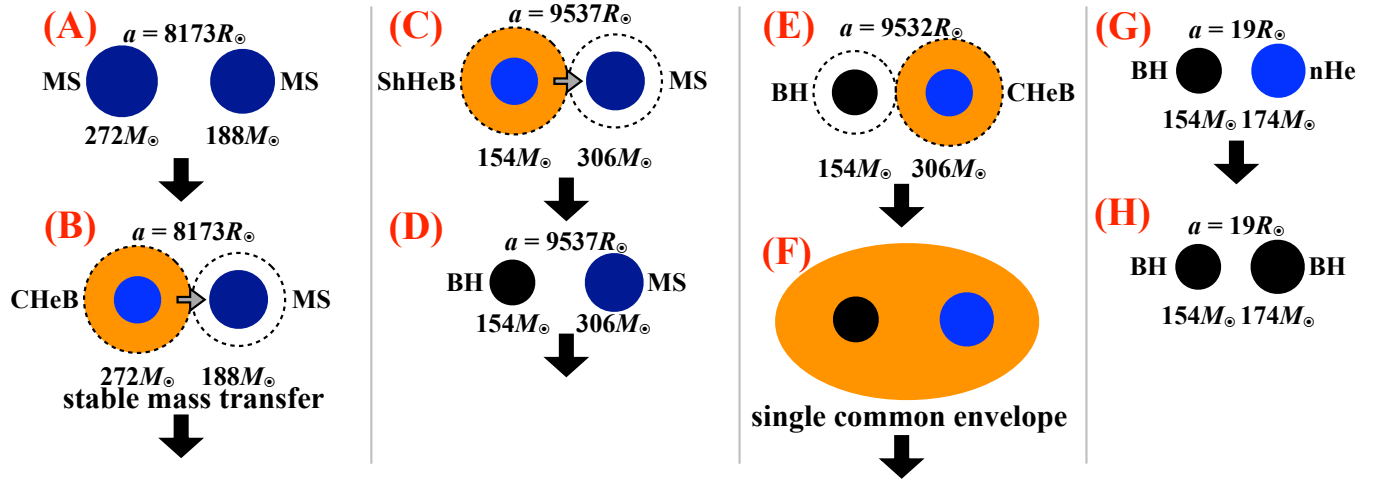


**Figure 3.** An example of “single common envelope channel (2)” when  $\alpha\lambda = 0.01$ . “ShHeB” stands for the shell helium burning phase.

### 3.1.2 primary BH mass distribution

The primary BH mass distributions of “high mass + high mass” BBH mergers which merge within a Hubble time are shown in Figure 4. For simplicity, we only show models with  $\gamma_1 = 0.0$ , but models with  $\gamma_1 = 1.0$  also have a similar distribution. The most distinctive feature is that the primary BH mass distributions have an upper limit. This upper limit decreases as the common envelope parameter  $\alpha\lambda$  increases. The reason for this is as follows. If the ZAMS mass of Pop. III stars is larger than  $\sim 600M_\odot$ , they expand extremely, become a red super giant, and have a convective envelope when they still in their MS phase. Therefore, if such a massive Pop. III MS star fills its Roche lobe, the mass transfer may be unstable, and the binary system enters a common envelope phase. After that, the binary system always coalesces because the core–envelope structure of MS star is not clear, and it will no longer evolve to a BBH. In order to avoid this common envelope episode, the initial orbital separation needs to be large enough.

Hereafter, in order to understand why there is an upper limit on the primary ZAMS mass of merging “high mass + high mass” BBHs, we consider the dependence of the merging timescale of the binary system on the primary ZAMS mass. The merging timescale  $t$  is proportional to  $a^4 m_{\text{BH,p}}^{-1} m_{\text{BH,s}}^{-1} m_{\text{tot}}^{-1}$ , where  $a$  is the orbital separation when BBH system is formed,  $m_{\text{BH,p}}$  is the primary BH mass,  $m_{\text{BH,s}}$  is the secondary BH mass and  $m_{\text{tot}}$  is the total mass of the BBH. Here, if we fix the secondary BH mass,  $m_{\text{BH,s}}$ , then the merging timescale  $t$  is roughly proportional to  $a^4 m_{\text{BH,p}}^{-2}$ . The orbital separation,  $a$ , is proportional to the radius  $r$  of a Pop. III giant star heavier than  $\approx 600M_\odot$ , and the primary BH mass,  $m_{\text{BH,p}}$ , is proportional to the ZAMS mass,  $m$ . Since there is the relation  $r \propto m^{0.6}$ ,  $t \propto m^{0.4}$ . Therefore, as the primary ZAMS mass increases, the merging timescale also increases, and exceeds a Hubble time at a critical ZAMS mass. That is why there is an upper limit on the primary ZAMS mass of merging BBHs.

If the value of  $\alpha\lambda$  is smaller, the efficiency of envelope stripping through common envelope gets lower, and thus the binary system can shrink more during the common envelope phase. Therefore, the more massive Pop. III stars can merge within a Hubble time with the smaller  $\alpha\lambda$ , and the upper limit of primary BH mass increases when the value of  $\alpha\lambda$  decreases.

### 3.1.3 mass ratio distribution

The mass ratio distributions of “high mass + high mass” BBH mergers which merge within a Hubble time are shown in Figure 5. When  $\alpha\lambda \gtrsim 0.5$ , “high mass + high mass” BBH mergers with the mass ratio  $> 0.8$  and  $< 0.8$  are formed through “contact common envelope channel” and “double common envelope channel”, respectively. If the binary is initially symmetric (initial mass ratio  $\gtrsim 0.8$ ), the evolutionary timescale is similar to each other and initially lighter star fills its Roche lobe while the initially heavier star fills its Roche lobe and stable mass transfer proceeds. After that, a “contact common envelope” occurs, only helium cores remain and the binary system becomes a binary naked helium star. Since the helium core mass ratio is roughly equal to initial mass ratio, the mass ratio of BBH formed through “contact common envelope channel” is  $\gtrsim 0.8$ .

If the initial mass ratio is  $\lesssim 0.8$ , the evolutionary timescale of both stars are somewhat different. Therefore, while the initially heavier star fills its Roche lobe and stable mass transfer proceeds, the initially lighter star does not yet expand significantly. After the initially lighter star becomes the post MS star but before it fills its Roche lobe, the initially heavier star evolves and its envelope becomes a convective, and then the binary system enters a common envelope phase. Like “contact common envelope channel”, the binary system becomes a binary naked helium star after the common envelope phase, and thus the mass ratio of BBHs formed through “double common envelope channel” is roughly same as initial mass ratio. If the initial mass ratio gets smaller, the wider orbital separation is needed for “double common envelope channel”. The reason is as follows. In order to cause a “double common envelope”, the initially heavier star fills its Roche lobe after the initially lighter star becomes a giant. If the initial mass ratio gets smaller, the difference between each evolutionary timescale gets larger, and thus the initially lighter star takes a relatively longer period to become a giant star. In order for the initially heavier star not to fill its Roche lobe during this relatively longer period, the wider initial orbital separation is needed. If the initial orbital separation is too wide, the delay time exceeds a Hubble time. In this way the minimum mass ratio of BBHs formed through “double common envelope channel” is determined. If the  $\alpha\lambda$  gets larger, the orbital separation just after the common envelope gets wider (see Equation 5), and thus the minimum mass ratio gets larger. When  $\alpha\lambda = 0.1$ , unlike the  $\alpha\lambda \gtrsim 0.5$  case, there are “high mass + high mass” BBHs formed through “single common envelope

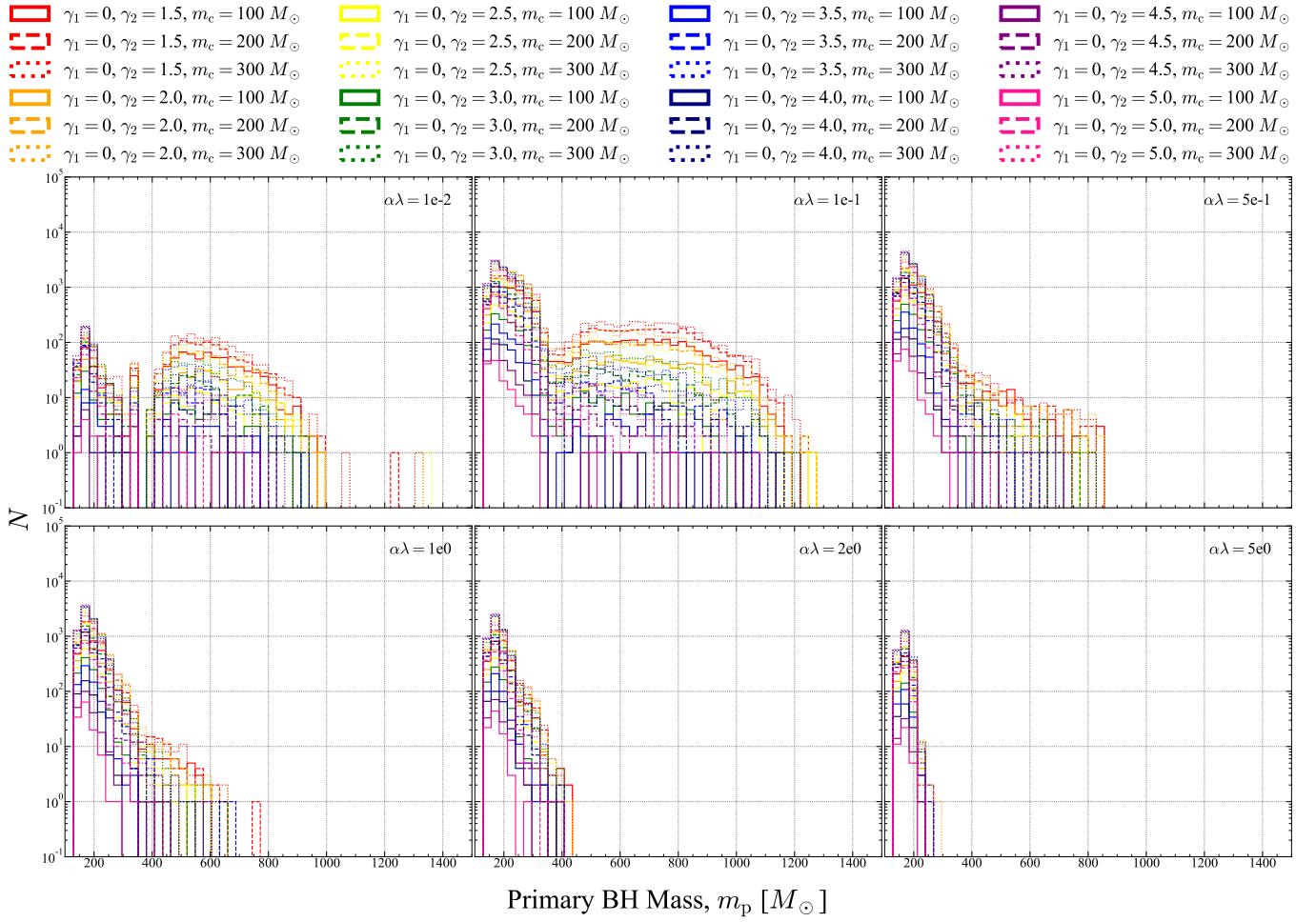


**Figure 4.** The primary BH mass distributions of “high mass + high mass” BBH mergers which merge within a Hubble time. From the upper left to upper right panel,  $\alpha\lambda = 0.01, 0.1$  and  $0.5$ , and from the lower left to lower right panel,  $\alpha\lambda = 1.0, 2.0$  and  $5.0$ . Each line corresponds to each IMF model. The normal lines and relatively transparent lines correspond to  $\gamma_1 = 0.0$  and  $1.0$ , respectively. The red, orange, yellow, green, blue, navy, purple and pink lines correspond to  $\gamma_2 = 1.5, 2.0, 2.5, 3.0, 3.5, 4.0, 4.5$  and  $5.0$ , respectively. The solid, dashed and dotted lines correspond to  $m_{\text{crit}} = 100M_\odot, 200M_\odot$  and  $300M_\odot$ , respectively.

channel (2)”, but the mechanism determining the minimum value of mass ratio  $q$  is the same. When  $\alpha\lambda = 0.01$ , all “high mass + high mass” BBHs which merge within a Hubble time are formed through “single common envelope channel (2)” (see Figure 3). Almost all “high mass + high mass” BBHs are mass inverted for  $\alpha\lambda = 0.01$ , and have the mass ratio  $q$  roughly equal to the ratio of the helium core mass of initially heavier star to the helium core mass of initially lighter star which gains significant mass from the initially heavier star (phase B in Figure 3). Therefore, as the initial mass ratio increases, the mass ratio  $q$  decreases. Since the initial mass ratio has an upper limit ( $= 1$ ), the mass ratio  $q$  also has lower limit.

### 3.1.4 effective spin distribution

The effective spin distributions of “high mass + high mass” BBH mergers which merge within a Hubble time are shown in Figure 6. The effective spin,

$$\chi_{\text{eff}} = \frac{m_{\text{BH,p}}\vec{\chi}_{\text{BH,p}} + m_{\text{BH,s}}\vec{\chi}_{\text{BH,s}}}{m_{\text{BH,p}} + m_{\text{BH,s}}} \cdot \frac{\vec{L}_{\text{orb}}}{|\vec{L}_{\text{orb}}|}, \quad (12)$$

is the mass weighted average of the dimensionless spin components perpendicular to the orbital plane. Here,  $m_{\text{BH,p}}$  and  $m_{\text{BH,s}}$  are the primary and secondary BH mass,  $\vec{\chi}_{\text{BH,p}}$  and  $\vec{\chi}_{\text{BH,s}}$  are the primary

and secondary BH spin vector and  $\vec{L}_{\text{orb}}$  is the orbital angular momentum vector. Since we do not assume that the kick is imparted during the BH formation in this study, BHs always aligned with the orbital angular momentum vector. Therefore, the effective spin can be written as

$$\begin{aligned} \chi_{\text{eff}} &= \frac{m_{\text{BH,p}}\chi_{\text{BH,p}} + m_{\text{BH,s}}\chi_{\text{BH,s}}}{m_{\text{BH,p}} + m_{\text{BH,s}}} \\ &= \frac{\chi_{\text{BH,p}} + q\chi_{\text{BH,s}}}{1 + q}. \end{aligned} \quad (13)$$

When  $\alpha\lambda \gtrsim 0.5$ , the “high mass + high mass” BBH mergers are formed through “contact common envelope channel” or “double common envelope channel”. Through these channels, both stars lose their hydrogen envelope during the common envelope phase and lose spin angular momenta at the same time. Therefore, both BHs have very low spin ( $\sim 0$ ) and the effective spin distribution sharply peaks at 0. If the orbital separation after the common envelope phase is too short, the naked helium star can be spun up by tidal interaction. In such a case, BHs have a non-zero spin and the effective spin of BBH mergers have a non-zero value. If  $\alpha\lambda$  gets larger, the orbital separation after the common envelope gets relatively wider, and the degree of spin-up by tidal interaction gets smaller. Therefore, the maximum effective spin gets smaller when  $\alpha\lambda$  gets larger. When

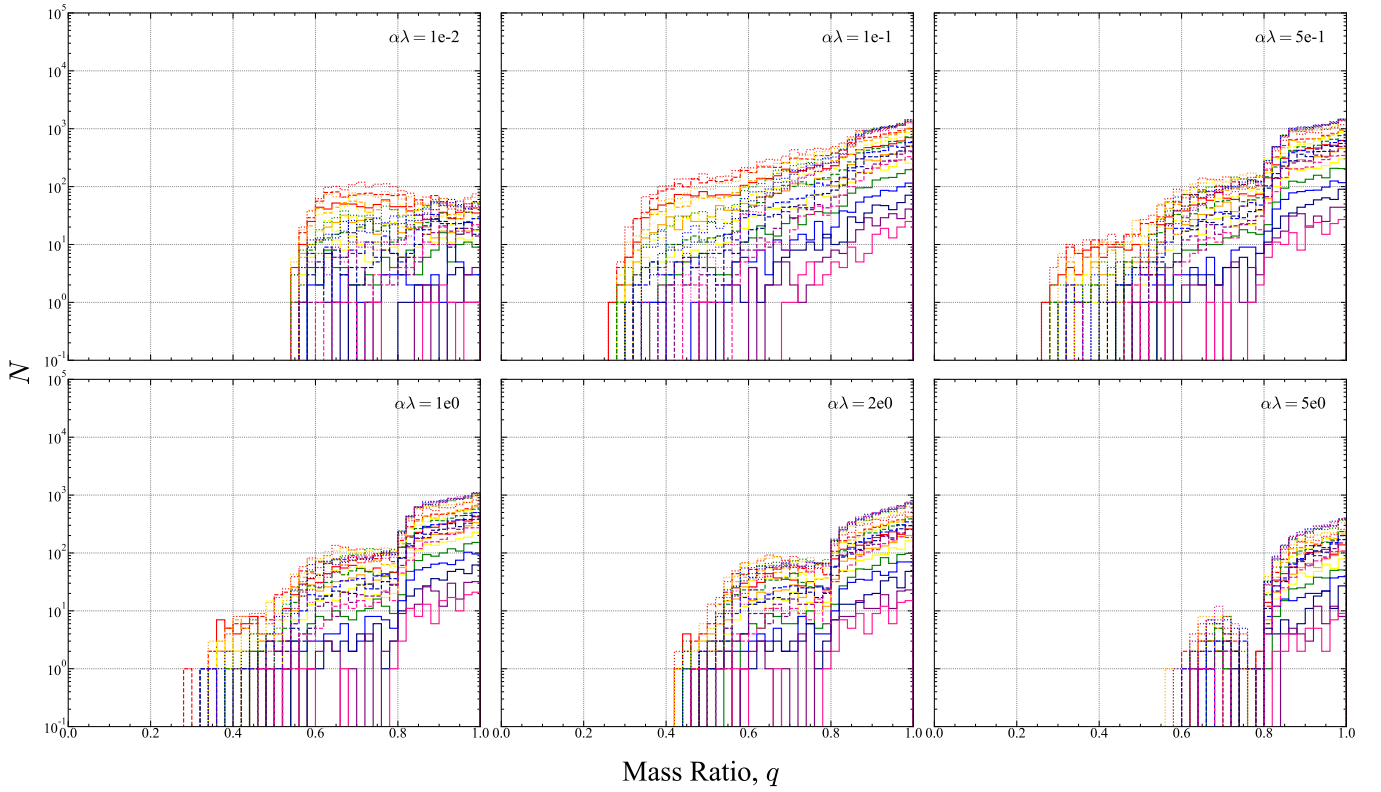


**Figure 5.** The mass ratio distributions of “high mass + high mass” BBH mergers which merge within a Hubble time. From the upper left to upper right panel,  $\alpha\lambda = 0.01, 0.1$  and  $0.5$ , and from the lower left to lower right panel,  $\alpha\lambda = 1.0, 2.0$  and  $5.0$ . The legends are same as that of Figure 4.

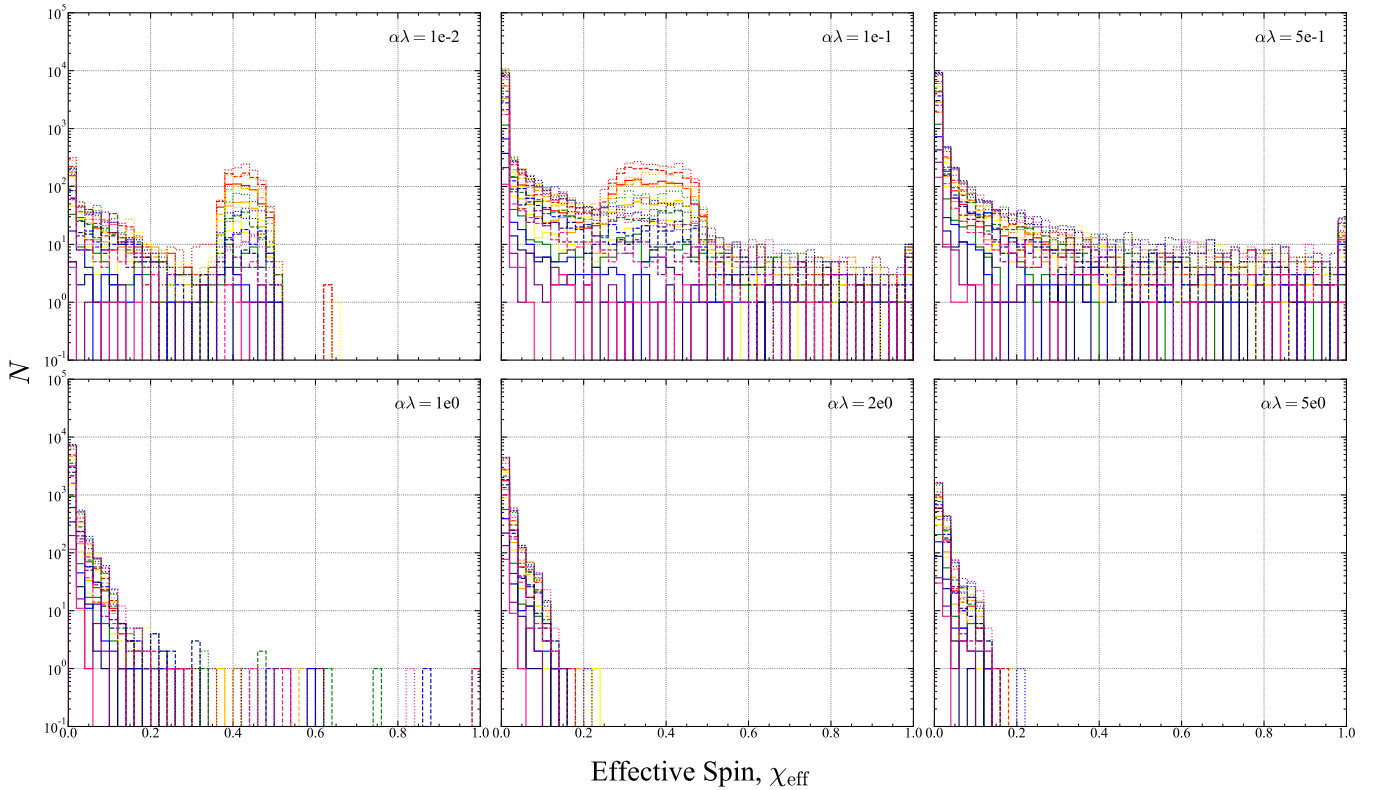


**Figure 6.** The effective spin distribution of “high mass + high mass” BBH mergers which merge within a Hubble time. From the upper left to upper right panel,  $\alpha\lambda = 0.01, 0.1$  and  $0.5$ , and from the lower left to lower right panel,  $\alpha\lambda = 1.0, 2.0$  and  $5.0$ . The legends are same as that of Figure 4.



$\alpha\lambda < 0.1$ , BBH mergers formed through “single common envelope (2)” emerges. Through this channel, the progenitor of one of the BH lose its hydrogen envelope by the common envelope, and thus this BH have a very low spin ( $\sim 0$ ). On the other hand, the progenitor of the other BH did not undergo a significant mass loss process, and thus the spin of this BH is high ( $\sim 1$ ). Therefore, the effective spin is written as

$$\chi_{\text{eff}} \sim \frac{q}{1+q} \in [0, 0.5]. \quad (14)$$

Therefore, the effective spin distribution of “high mass + high mass” BBH mergers assemble around non-zero value, 0.35–0.5 for  $\alpha\lambda = 0.01$  and 0.25–0.5 for  $\alpha\lambda = 0.1$ .

### 3.1.5 delay time distribution

The delay time distributions of “high mass + high mass” BBH mergers which merge within a Hubble time are shown in Figure 7. The delay time  $t_d$  is roughly proportional to  $a^4 m_{\text{BH,p}}^{-1} m_{\text{BH,s}}^{-1} m_{\text{tot}}^{-1}$ . If the  $\alpha\lambda$  gets larger, the orbital separation after the common envelope gets wider, and thus the delay time gets longer. Therefore, the minimum delay time increases when  $\alpha\lambda$  gets larger, and exceeds 10 and 100 Myr when  $\alpha\lambda = 2.0$  and 5.0. When the value of  $\alpha\lambda$  is too small such as 0.01, the orbital separation after the common envelope is too short, and thus the maximum delay time is lower than 100 Myr.

### 3.1.6 merger rate density

The redshift evolution of “high mass + high mass” BBH merger rate density is shown in Figure 8. The merger rate densities roughly trace the star formation rate history (de Souza et al. 2011), and the peaks of merger rate densities are located near the redshift  $z \sim 10$ . However, when  $\alpha\lambda = 2.0$ , the minimum delay time exceeds 10 Myr, hence the peak of merger rate density is shifted toward low redshift compared to that of  $\alpha\lambda \lesssim 1.0$ . When  $\alpha\lambda = 5.0$ , the minimum delay time exceeds 100 Myr, hence the peak of merger rate density is significantly shifted toward low redshift compared to other cases. Furthermore, the merger rate density becomes significantly smaller at the redshift  $z \gtrsim 15$ –20. When  $\alpha\lambda = 0.01$ , the maximum delay time is so short that the merger rate density rapidly decreases after the end of Pop. III star formation. Therefore, the merger rate densities are strictly 0 when  $z \lesssim 3$ .

## 3.2 low mass + high mass

### 3.2.1 formation channel

The almost all “low mass + high mass” BBH mergers are formed through “single common envelope channel (2)”, and example formation channel is shown in Figure 9. Both stars would cause the pair-instability supernova if they were not in the binary system, but thanks to the binary interaction such as stable mass transfer one of the star gains the mass and becomes a “high mass BH”. On the other hand, the other star loses the mass and becomes a “low mass BH”. In order to significantly transfer the stellar mass to avoid the pair-instability supernova, the mass transfer rate needs to be high and the initial orbital separation needs to be short. If the initial orbital separation is short and  $\alpha\lambda$  is smaller, the binary system coalesces after the common envelope phase, and thus “low mass + high mass” BBH mergers cannot be formed when  $\alpha\lambda \lesssim 0.5$ .

### 3.2.2 primary BH mass distribution

The primary BH mass distributions of “low mass + high mass” BBH mergers which merge within a Hubble time are shown in Figure 10. The primary BH mass distributions are almost same for the different  $\alpha\lambda$  values. Since both stars are initially 100–200  $M_{\odot}$  and the progenitor of primary BH can only increase its mass up to  $\sim 300M_{\odot}$ , the primary BH mass is from 135  $M_{\odot}$  to  $\sim 200M_{\odot}$ . 135  $M_{\odot}$  is the upper end of pair-instability mass gap in this study.

### 3.2.3 mass ratio distribution

The mass ratio distributions of “low mass + high mass” BBH mergers which merge within a Hubble time are shown in Figure 11. The mass ratio distributions are roughly same for the different  $\alpha\lambda$  values. The maximum mass ratio is equal to the ratio of lower end of pair-instability mass gap ( $= 45M_{\odot}$ ) to the upper end ( $= 135M_{\odot}$ ), so that 0.33. When the  $\alpha\lambda = 2.0$  and 5.0, the orbital separation does not shrink much through common envelope phase compared to when  $\alpha\lambda = 1.0$ . Therefore, the initially shorter orbital separation are allowed for  $\alpha\lambda = 2.0$  and 5.0, and in these cases the stellar mass is transferred more significantly (phase B and D in Figure 9). That is why minimum mass ratio gets lower when  $\alpha\lambda = 2.0$  and 5.0.

### 3.2.4 effective spin distribution

The effective spin distributions of “low mass + high mass” BBH mergers which merge within a Hubble time are shown in Figure 12. The progenitor of secondary BH loses its spin angular momentum through significant mass transfer process (phase B and D in Figure 9), and thus the BH also has very low spin ( $\sim 0$ ). The progenitor of the primary BH also loses its spin angular momentum during the common envelope phase (phase G in Figure 9). However, the orbital separation after the common envelope is so short that the progenitor of the primary BH is highly spun up by tidal interaction. Thus, the spin of primary BH is high. As the value of  $\alpha\lambda$  increases, the degree of spin-up decreases, and thus the effective spin distribution shifted toward lower value.

### 3.2.5 delay time distribution

The delay time distribution of “low mass + high mass” BBH mergers which merge within a Hubble time are shown in Figure 13. As the value of  $\alpha\lambda$  increases, the orbital separation after the common envelope widens, and thus the delay time distribution shifted toward the higher value. Since the initial orbital separation is short in order to form “low mass + high mass” BBHs, the delay time also becomes short, and does not exceeds  $10^3$  Myr for  $\alpha\lambda = 1.0, 2.0$  and 5.0.

### 3.2.6 merger rate density

The redshift evolution of “low mass + high mass” BBH merger rate density is shown in Figure 14. The merger rate densities roughly trace the star formation rate history (de Souza et al. 2011), and the peaks of merger rate densities are located near the redshift  $z \sim 10$ . However, when  $\alpha\lambda = 5.0$ , the minimum delay time exceeds 10 Myr, hence the peak of merger rate density is shifted toward low redshift compared to that of  $\alpha\lambda \lesssim 2.0$ . The maximum delay time is so short that the merger rate density rapidly decreases after the end of Pop. III star formation. Therefore, the merger rate densities are strictly 0 when  $z \lesssim 3$ .

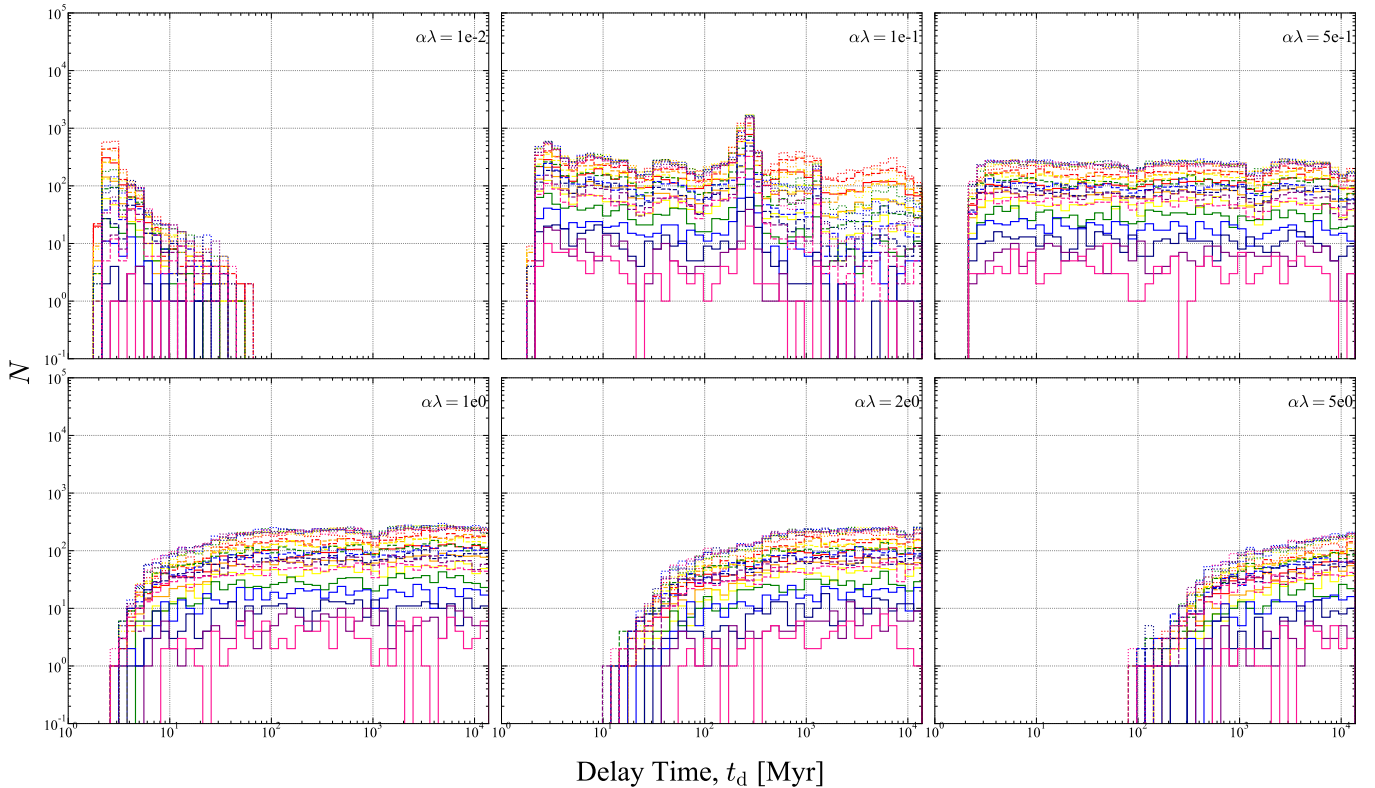


**Figure 7.** The delay time distributions of “high mass + high mass” BBH mergers which merge within a Hubble time. From the upper left to upper right panel,  $\alpha\lambda = 0.01, 0.1$  and  $0.5$ , and from the lower left to lower right panel,  $\alpha\lambda = 1.0, 2.0$  and  $5.0$ . The legends are same as that of Figure 4.

## 4 DISCUSSION

So far, the BBH mergers with IMBHs have not been discovered by GW observation. Thus, the upper limit on the merger rate density of the BBH mergers with IMBHs is obtained, and the value is  $\sim 0.01 \text{ Gpc}^{-3} \text{ yr}^{-1}$  (The LIGO Scientific Collaboration et al. 2021a; Ezquiaga & Holz 2021). In Section 4.1, we compare the merger rate density of BBHs with IMBHs with this upper limit and investigate what parameter set meets the criterion obtained from the non-detection. In Section 4.2, using these parameter sets, we infer the detection rate by future GW detectors. Furthermore, we show the likelihood ratio for each model assuming a BBH with IMBHs is observed and explain how we can limit the value of  $\alpha\lambda$  and IMF models.

### 4.1 comparison with the current GW observation

The merger rate density of BBHs with IMBHs at the redshift  $z = 0$  are shown in Table 2–6 for  $\alpha\lambda = 0.1$ – $5.0$ . The value lower than the upper limit,  $0.01 \text{ Gpc}^{-3} \text{ yr}^{-1}$ , is written in bold. The BBHs with IMBHs are classified as “high mass + high mass” BBHs and “low mass + high mass” BBHs. The merger rate density of “low mass + high mass” BBHs is 0 at the redshift  $z = 0$  (see Section 3.2.6), hence the merger rate density shown in the Table 2–6 are that of “high mass + high mass” BBH mergers. When  $\alpha\lambda = 0.01$ , the merger rate density of “high mass + high mass” BBHs is also 0 at the redshift  $z = 0$  (see Section 3.1.6), hence the merger rate density of BBHs with IMBHs is strictly 0.

Since the delay time is so short that the Pop. III BBHs with IMBHs cannot merge at the local Universe and the merger rate is 0 when

$\alpha\lambda = 0.01$ , any IMF is allowed. Therefore it is impossible to impose any restrictions on Pop. III IMF. When  $\alpha\lambda = 0.1$ , the contribution from the Pop. III star heavier than  $\sim 400 M_{\odot}$  is significant. Therefore, an IMF with the sufficiently large  $\gamma_2$  is allowed for  $\gamma_1 = 0$  and 1 and  $m_{\text{crit}} = 100$ – $300 M_{\odot}$  (see Table 2). When  $\alpha\lambda \gtrsim 0.5$ , the contribution from the Pop. III star  $\sim 200 M_{\odot}$  is significant. In this study, the Pop. III IMF is relatively top heavy below the critical mass  $m_{\text{crit}}$ . Therefore, when  $m_{\text{crit}} = 200$  and  $300 M_{\odot}$ , it is impossible to decrease the merger rate density by steeping the IMF slope (i.e., increasing the value of  $\gamma_2$ ) above the critical mass, and thus the Pop. III IMF with  $m_{\text{crit}} = 200$  and  $300 M_{\odot}$  are not allowed (see Table 3–6).

### 4.2 future observation

#### 4.2.1 detection rate

In this section, we compute the detection rate by the second generation GW detector, advanced LIGO (O4), third generation detector, Einstein telescope and the space-borne detector, LISA for the models which meet the upper limit from the non-detection. Figure 15 shows the horizon of each detector. The detection rate of BBHs with IMBHs by advanced LIGO (O4), Einstein telescope and LISA are shown in Table 7–12 for  $\alpha\lambda = 0.01$ – $5.0$ . The detection rate by advanced LIGO (O4), Einstein telescope and LISA are written in roman, italic and bold font, respectively.

Next, we choose the IMF model with the highest detection rate for each detector and for each  $\alpha\lambda$ , and show the detection rate as a function of mass. If we choose different IMF model, the mass distribution does not change significantly. Therefore, it is sufficient

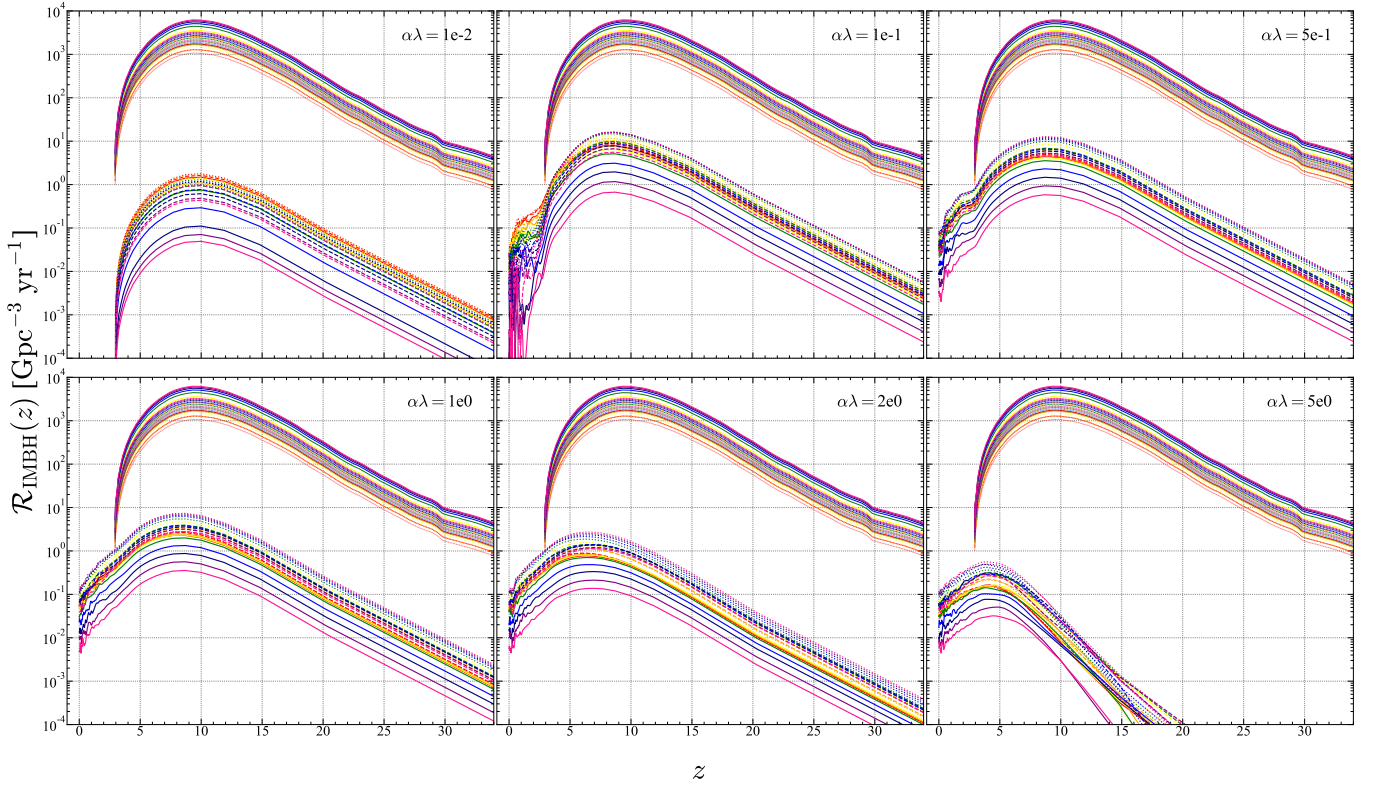


**Figure 8.** The redshift evolution of merger rate density of “high mass + high mass” BBH mergers. From the upper left to upper right panel,  $\alpha\lambda = 0.01, 0.1$  and  $0.5$ , and from the lower left to lower right panel,  $\alpha\lambda = 1.0, 2.0$  and  $5.0$ . The legends are same as that of Figure 4. The lines at the bottom of each panel are the redshift evolution of BBH merger rate density. The relatively thin lines at the top of each panel indicate the binary formation rate [ $\text{Gpc}^{-3} \text{yr}^{-1}$ ]. The binary formation rate is the number density of Pop. III binaries born at each redshift and is calculated from star formation rate.

**Table 2.** The merger rate density [ $\text{Gpc}^{-3} \text{yr}^{-1}$ ] of BBHs with IMBHs at the redshift  $z = 0$  for  $\alpha\lambda = 0.1$ . The value lower than the upper limit,  $0.01 \text{Gpc}^{-3} \text{yr}^{-1}$ , is written in bold.

$\gamma_1$	$m_{\text{crit}} [M_{\odot}]$	$\gamma_2$								
		1.5	2.0	2.5	3.0	3.5	4.0	4.5	5.0	
0.0	100	2.44e-02	1.09e-02	<b>9.83e-03</b>	1.23e-02	<b>3.12e-03</b>	<b>4.77e-03</b>	<b>2.40e-04</b>	<b>3.79e-04</b>	
0.0	200	1.82e-02	2.33e-02	1.42e-02	2.29e-02	1.34e-02	<b>6.04e-03</b>	<b>8.70e-03</b>	<b>2.38e-03</b>	
0.0	300	2.29e-02	2.74e-02	2.91e-02	2.60e-02	2.30e-02	1.50e-02	<b>9.06e-03</b>	<b>9.98e-03</b>	
1.0	100	2.69e-02	1.36e-02	1.43e-02	<b>6.08e-03</b>	<b>8.34e-03</b>	<b>1.50e-04</b>	<b>8.01e-04</b>	<b>5.68e-05</b>	
1.0	200	2.42e-02	2.08e-02	1.86e-02	<b>1.60e-03</b>	<b>6.40e-03</b>	<b>2.74e-03</b>	<b>2.41e-03</b>	<b>1.79e-03</b>	
1.0	300	2.18e-02	1.49e-02	1.91e-02	1.29e-02	1.08e-02	<b>8.18e-03</b>	<b>9.28e-03</b>	<b>7.72e-03</b>	

**Table 3.** Same as Table 2 but for  $\alpha\lambda = 0.5$ .

$\gamma_1$	$m_{\text{crit}} [M_{\odot}]$	$\gamma_2$								
		1.5	2.0	2.5	3.0	3.5	4.0	4.5	5.0	
0.0	100	3.97e-02	3.77e-02	3.79e-02	3.38e-02	1.38e-02	<b>8.73e-03</b>	<b>6.69e-03</b>	<b>3.16e-03</b>	
0.0	200	4.37e-02	5.06e-02	5.33e-02	4.76e-02	3.99e-02	4.95e-02	3.81e-02	3.04e-02	
0.0	300	5.43e-02	6.29e-02	7.86e-02	7.33e-02	8.46e-02	7.89e-02	7.03e-02	9.14e-02	
1.0	100	3.80e-02	3.95e-02	2.67e-02	1.93e-02	<b>9.67e-03</b>	<b>7.76e-03</b>	<b>4.48e-03</b>	<b>2.09e-03</b>	
1.0	200	4.28e-02	3.89e-02	3.57e-02	4.34e-02	3.19e-02	2.36e-02	2.10e-02	1.31e-02	
1.0	300	3.95e-02	4.72e-02	4.85e-02	6.53e-02	6.30e-02	4.98e-02	5.99e-02	4.95e-02	

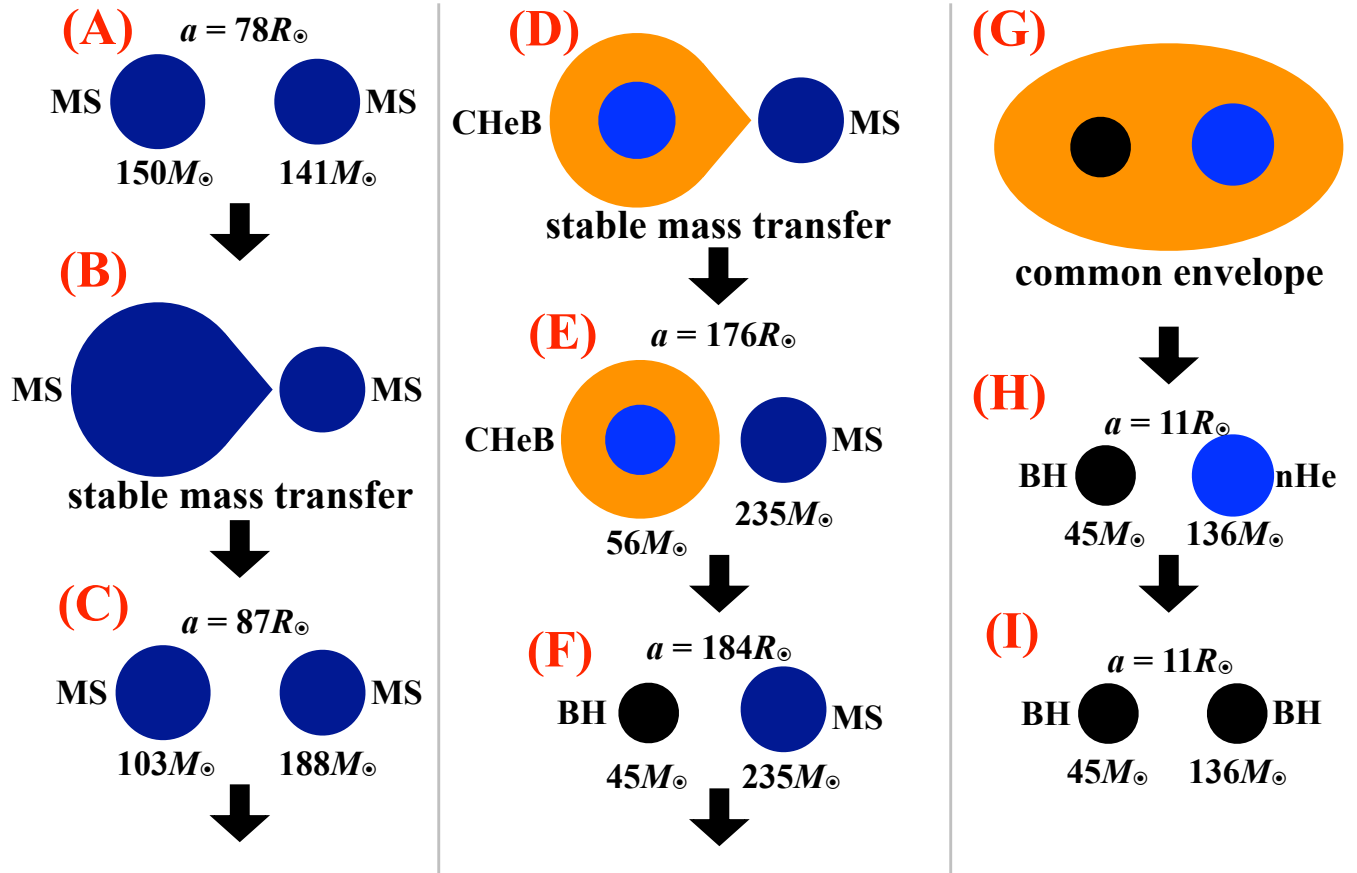


**Figure 9.** The example channel of “low mass + high mass” when  $\alpha\lambda = 1.0$ .

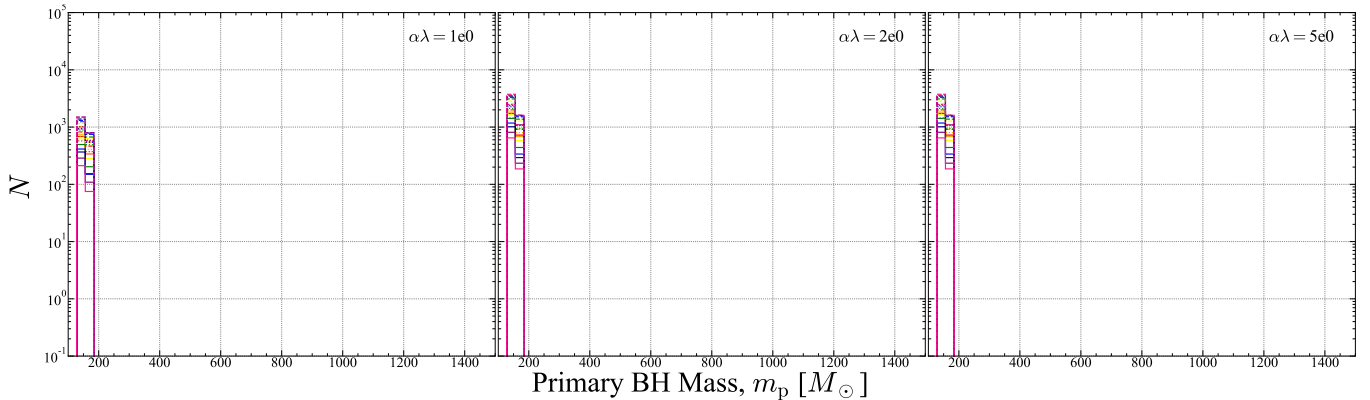


**Figure 10.** The primary BH mass distribution of “low mass + high mass” BBH mergers which merge within a Hubble time. From the left to right panel,  $\alpha\lambda = 1.0, 2.0$  and  $5.0$ . The legends are same as that of Figure 4.

to show the mass distribution of one IMF model for each detector and for each  $\alpha\lambda$ .

The detection rate by advanced LIGO (O4) are shown in Figure 16. The IMF models with the highest detection rate by advanced LIGO (O4) are  $(\gamma_1 = 0.0, \gamma_2 = 1.5, m_{\text{crit}} = 100M_{\odot})$ ,  $(\gamma_1 = 0.0, \gamma_2 = 5.0, m_{\text{crit}} = 300M_{\odot})$ ,  $(\gamma_1 = 0.0, \gamma_2 = 4.0, m_{\text{crit}} = 100M_{\odot})$ ,  $(\gamma_1 = 1.0, \gamma_2 = 4.5, m_{\text{crit}} = 100M_{\odot})$  and  $(\gamma_1 = 0.0, \gamma_2 = 4.0, m_{\text{crit}} = 100M_{\odot})$  for  $\alpha\lambda = 0.01, 0.1, 0.5, 1.0, 2.0$  and  $5.0$ . When the value of  $\alpha\lambda$  is small,

the delay time is also short. Therefore, BBHs with IMBHs are hard to be detected by the advanced LIGO with the horizon  $z \sim 1$ . On the other hand, when  $\alpha\lambda$  is larger than 0.5, BBH with IMBHs merges within  $z \sim 1$ , and the advanced LIGO have a potential to detect the BBHs with total mass  $\sim 300M_{\odot}$  and mass ratio  $\sim 1$ .

The detection rate by Einstein telescope are shown in Figure 17. The IMF models with the highest detection rate by Einstein telescope are  $(\gamma_1 = 0.0, \gamma_2 = 4.5, m_{\text{crit}} = 300M_{\odot})$ ,  $(\gamma_1 = 0.0, \gamma_2 = 5.0, m_{\text{crit}} = 300M_{\odot})$ ,  $(\gamma_1 = 1.0, \gamma_2 = 3.5, m_{\text{crit}} = 100M_{\odot})$ ,



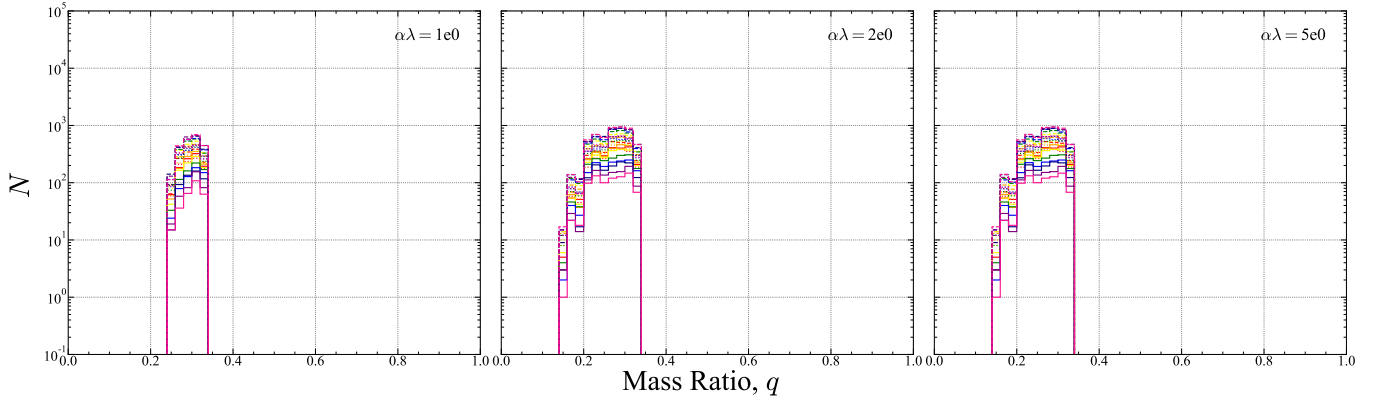


**Figure 11.** The mass ratio distribution of “low mass + high mass” BBH mergers which merge within a Hubble time. From the left to right panel,  $\alpha\lambda = 1.0, 2.0$  and  $5.0$ . The legends are same as that of Figure 4.

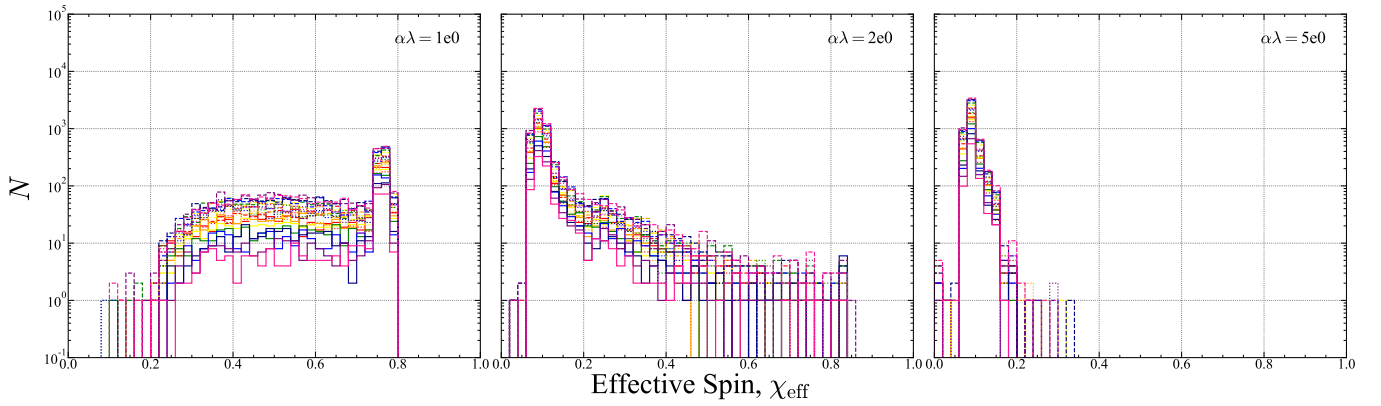


**Figure 12.** The effective spin distribution of “low mass + high mass” BBH mergers which merge within a Hubble time. From the left to right panel,  $\alpha\lambda = 1.0, 2.0$  and  $5.0$ . The legends are same as that of Figure 4.

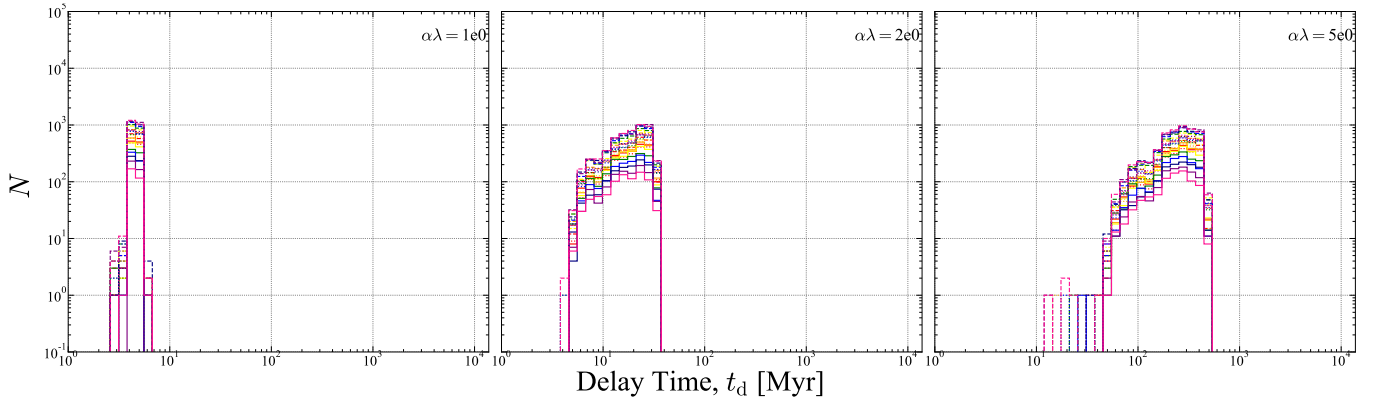


**Figure 13.** The delay time distribution of “low mass + high mass” BBH mergers which merge within a Hubble time. From the left to right panel,  $\alpha\lambda = 1.0, 2.0$  and  $5.0$ . The legends are same as that of Figure 4.

( $\gamma_1 = 0.0, \gamma_2 = 5.0, m_{\text{crit}} = 100M_{\odot}$ ), ( $\gamma_1 = 0.0, \gamma_2 = 5.0, m_{\text{crit}} = 100M_{\odot}$ ) and ( $\gamma_1 = 0.0, \gamma_2 = 4.0, m_{\text{crit}} = 100M_{\odot}$ ) for  $\alpha\lambda = 0.01, 0.1, 0.5, 1.0, 2.0$  and  $5.0$ . Einstein telescope can detect a BBH merger up to  $z \sim 10\text{--}100$  (see Figure 15). The total mass and mass ratio of observable “high mass + high mass” BBHs are  $\sim 300M_{\odot}$  and  $\sim 1$ , respectively. When  $\alpha\lambda$  is larger than 1, “low mass + high mass” BBH mergers can occur (see Section refsubsec: lh), and can be detected

by Einstein telescope. Their total mass and mass ratio are  $\sim 200M_{\odot}$  and  $\sim 0.2$ , respectively. The detection rate by Cosmic Explorer is roughly same as that by Einstein telescope.

The detection rate by LISA are shown in Figure 18. The IMF models with the highest detection rate by LISA are ( $\gamma_1 = 0.0, \gamma_2 = 1.5, m_{\text{crit}} = 300M_{\odot}$ ), ( $\gamma_1 = 0.0, \gamma_2 = 2.5, m_{\text{crit}} = 100M_{\odot}$ ), ( $\gamma_1 = 1.0, \gamma_2 = 3.5, m_{\text{crit}} = 100M_{\odot}$ ), ( $\gamma_1 = 1.0, \gamma_2 = 4.5, m_{\text{crit}} =$

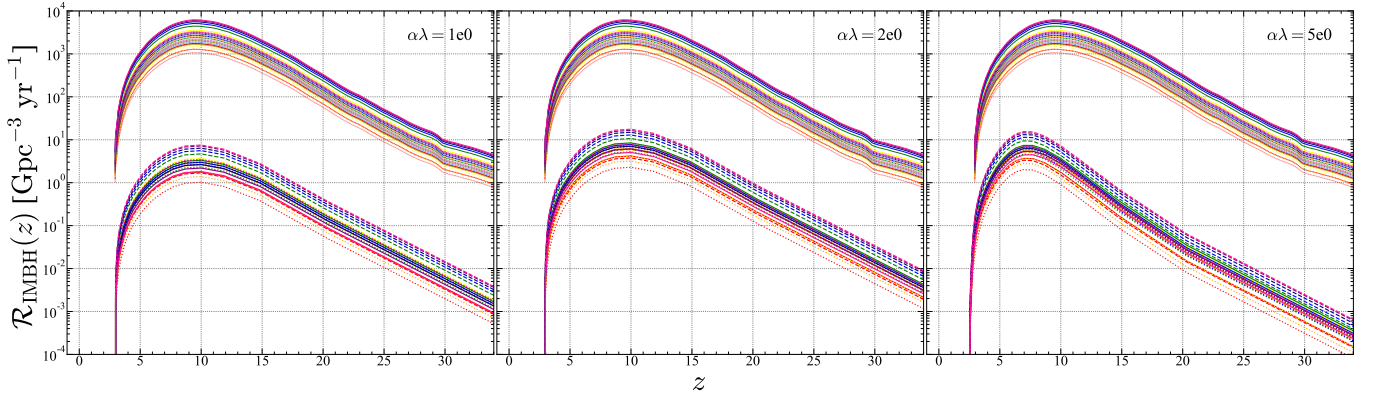


**Figure 14.** The redshift evolution of merger rate density of “low mass + high mass” BBH. From the left to right, for  $\alpha\lambda = 1.0, 2.0$  and  $5.0$ . The legends are same as that of Figure 4. The lines at the bottom of each panel are the redshift evolution of BBH merger rate density. The relatively thin lines at the top of each panel indicate the binary formation rate [ $\text{Gpc}^{-3} \text{yr}^{-1}$ ].

**Table 4.** Same as Table 2 but for  $\alpha\lambda = 1.0$ .

$\gamma_1$	$m_{\text{crit}} [M_{\odot}]$	$\gamma_2$							
		1.5	2.0	2.5	3.0	3.5	4.0	4.5	5.0
0.0	100	5.32e-02	5.30e-02	4.16e-02	3.03e-02	2.51e-02	1.32e-02	1.03e-02	<b>4.85e-03</b>
0.0	200	5.68e-02	7.11e-02	6.59e-02	6.69e-02	6.61e-02	6.22e-02	5.57e-02	3.76e-02
0.0	300	5.92e-02	7.65e-02	9.86e-02	1.08e-01	1.16e-01	1.21e-01	1.17e-01	1.19e-01
1.0	100	4.19e-02	4.32e-02	3.90e-02	2.22e-02	1.59e-02	1.02e-02	<b>6.22e-03</b>	<b>3.90e-03</b>
1.0	200	5.04e-02	5.36e-02	3.86e-02	4.56e-02	4.56e-02	3.35e-02	3.69e-02	3.32e-02
1.0	300	4.85e-02	6.47e-02	7.73e-02	7.43e-02	7.41e-02	6.96e-02	7.63e-02	7.73e-02

**Table 5.** Same as Table 2 but for  $\alpha\lambda = 2.0$ .

$\gamma_1$	$m_{\text{crit}} [M_{\odot}]$	$\gamma_2$							
		1.5	2.0	2.5	3.0	3.5	4.0	4.5	5.0
0.0	100	4.28e-02	4.95e-02	4.76e-02	4.19e-02	2.05e-02	1.50e-02	1.00e-02	<b>5.87e-03</b>
0.0	200	4.92e-02	6.40e-02	7.69e-02	6.86e-02	6.32e-02	6.37e-02	5.83e-02	4.89e-02
0.0	300	5.19e-02	7.84e-02	8.36e-02	1.06e-01	1.13e-01	1.20e-01	1.13e-01	1.33e-01
1.0	100	4.27e-02	4.21e-02	3.67e-02	2.33e-02	1.79e-02	1.10e-02	<b>6.06e-03</b>	<b>3.30e-03</b>
1.0	200	5.44e-02	6.12e-02	5.09e-02	5.03e-02	4.99e-02	4.07e-02	4.03e-02	2.92e-02
1.0	300	5.48e-02	6.41e-02	6.45e-02	7.90e-02	7.25e-02	7.56e-02	8.26e-02	8.28e-02

$100M_{\odot}$ ), ( $\gamma_1 = 1.0, \gamma_2 = 4.5, m_{\text{crit}} = 100M_{\odot}$ ) and ( $\gamma_1 = 0.0, \gamma_2 = 4.0, m_{\text{crit}} = 100M_{\odot}$ ) for  $\alpha\lambda = 0.01, 0.1, 0.5, 1.0, 2.0$  and  $5.0$ . LISA can detect BBHs with total mass  $\sim 1000M_{\odot}$  up to  $z \sim 1000$ , but is hard to detect BBHs with total mass  $\sim 100M_{\odot}$  (see Figure 15). Since the maximum mass decreases when  $\alpha\lambda$  increases (see Section 3.1.2), BBHs with IMBHs are hard to be detected by LISA when  $\alpha\lambda$  is larger than 0.5. On the other hand, when  $\alpha\lambda$  is smaller than 0.1, BBHs with total mass  $\sim 1000M_{\odot}$  can form and merge. LISA can detect such very massive BBH mergers. The detection rate by Tianqin is roughly same as that by LISA.

#### 4.2.2 constraint on the models

From Table 7–12, Einstein telescope will be able to detect several tens to thousands BBHs with IMBHs in the future. Therefore, we may be able to impose restrictions on models by using mass distribution. On the other hand, advanced LIGO (O4) and LISA may only see one

to a few BBHs. Thus, in this section, in order to impose restrictions on the model when only one BBH with IMBHs is detected, we compute and show the likelihood ratio for each parameter ( $\alpha\lambda, \gamma_1, \gamma_2$  and  $m_{\text{crit}}$ ) assuming that one BBH with IMBHs with a certain total mass is observed by a certain detector. We simply assume that IMF models occurs with equal probability and  $\alpha\lambda$  have a probability density,  $p(\log(\alpha\lambda)) \propto \text{const}$ .

Figure 19 shows the likelihood ratio to the maximum likelihood for  $\alpha\lambda$ . For example, from Figure 19 (a), if a BBH with total mass  $\sim 500M_{\odot}$  are detected by advanced LIGO (O4), we can find that most likely model is  $\alpha\lambda = 0.5$  and about three times more likely than the second most likely model,  $\alpha\lambda = 0.1$ . As described in Section 3.1.2, the smaller  $\alpha\lambda$  value is, the larger the maximum primary BH mass. Therefore, as the detected BBH total mass increases,  $\alpha\lambda$  value with the maximum likelihood decreases. We can impose restrictions on  $\alpha\lambda$  to some degree if a BBH with total mass  $\geq 500M_{\odot}$  are detected by advanced LIGO (O4) or LISA.

**Table 6.** Same as Table 2 but for  $\alpha\lambda = 5.0$ .

$\gamma_1$	$m_{\text{crit}} [M_{\odot}]$	$\gamma_2$							
		1.5	2.0	2.5	3.0	3.5	4.0	4.5	5.0
0.0	100	3.32e-02	4.47e-02	3.36e-02	3.16e-02	1.90e-02	<b>9.64e-03</b>	<b>8.18e-03</b>	<b>6.29e-03</b>
0.0	200	3.59e-02	4.99e-02	6.03e-02	5.30e-02	5.99e-02	5.56e-02	5.61e-02	4.78e-02
0.0	300	4.39e-02	5.44e-02	7.18e-02	8.86e-02	1.03e-01	1.07e-01	1.01e-01	1.08e-01
1.0	100	3.73e-02	3.90e-02	3.33e-02	2.28e-02	1.39e-02	1.06e-02	<b>6.21e-03</b>	<b>2.76e-03</b>
1.0	200	3.12e-02	3.67e-02	4.56e-02	4.11e-02	4.06e-02	3.71e-02	2.95e-02	2.88e-02
1.0	300	3.96e-02	4.88e-02	4.80e-02	6.68e-02	7.08e-02	8.16e-02	7.09e-02	9.28e-02

**Table 7.** The detection rate [ $\text{yr}^{-1}$ ] of BBHs with IMBHs for  $\alpha\lambda = 0.01$ . The detection rate by advanced LIGO (O4), Einstein telescope and LISA are written in roman, *italic* and **bold** font, respectively. If an IMF model does not meet the upper limit from the non-detection, only “-” is written in the cell.

$\gamma_1$	$m_{\text{crit}} [M_{\odot}]$	$\gamma_2$							
		1.5	2.0	2.5	3.0	3.5	4.0	4.5	5.0
0.0	100	0.0	0.0	0.0	0.0	0.0	0.0	0.0	0.0
		<i>23.6</i>	<i>24.0</i>	<i>22.1</i>	<i>22.1</i>	<i>11.5</i>	<i>6.0</i>	<i>4.6</i>	<i>3.4</i>
		<b>213.8</b>	<b>140.7</b>	<b>79.3</b>	<b>79.3</b>	<b>21.8</b>	<b>5.4</b>	<b>1.4</b>	<b>1.0</b>
0.0	200	0.0	0.0	0.0	0.0	0.0	0.0	0.0	0.0
		<i>25.3</i>	<i>30.6</i>	<i>34.0</i>	<i>35.1</i>	<i>36.7</i>	<i>36.9</i>	<i>30.6</i>	<i>29.6</i>
		<b>240.5</b>	<b>192.4</b>	<b>115.2</b>	<b>87.0</b>	<b>54.1</b>	<b>27.5</b>	<b>15.4</b>	<b>7.8</b>
0.0	300	0.0	0.0	0.0	0.0	0.0	0.0	0.0	0.0
		<i>25.1</i>	<i>30.2</i>	<i>33.9</i>	<i>42.9</i>	<i>49.6</i>	<i>58.3</i>	<i>58.8</i>	<i>57.4</i>
		<b>263.3</b>	<b>231.9</b>	<b>170.3</b>	<b>125.6</b>	<b>93.5</b>	<b>64.6</b>	<b>38.5</b>	<b>32.4</b>
1.0	100	0.0	0.0	0.0	0.0	0.0	0.0	0.0	0.0
		<i>18.9</i>	<i>22.0</i>	<i>16.8</i>	<i>12.4</i>	<i>11.2</i>	<i>6.7</i>	<i>3.4</i>	<i>1.6</i>
		<b>197.3</b>	<b>138.5</b>	<b>71.2</b>	<b>32.6</b>	<b>17.1</b>	<b>3.3</b>	<b>3.4</b>	<b>0.0</b>
1.0	200	0.0	0.0	0.0	0.0	0.0	0.0	0.0	0.0
		<i>25.2</i>	<i>27.0</i>	<i>25.5</i>	<i>28.9</i>	<i>23.5</i>	<i>29.5</i>	<i>21.1</i>	<i>19.1</i>
		<b>228.0</b>	<b>160.4</b>	<b>104.8</b>	<b>46.6</b>	<b>37.6</b>	<b>23.2</b>	<b>9.1</b>	<b>6.4</b>
1.0	300	0.0	0.0	0.0	0.0	0.0	0.0	0.0	0.0
		<i>20.8</i>	<i>26.6</i>	<i>27.7</i>	<i>32.8</i>	<i>38.1</i>	<i>39.9</i>	<i>42.4</i>	<i>43.8</i>
		<b>240.3</b>	<b>174.9</b>	<b>137.9</b>	<b>85.1</b>	<b>68.0</b>	<b>39.5</b>	<b>30.0</b>	<b>15.9</b>

Figure 20–22 show the likelihood ratio of IMF parameters. It is hard to distinguish between  $\gamma_1 = 0.0$  and 1.0 (see Figure 20). If more massive BBH is detected, smaller  $\gamma_2$ , i.e., shallower IMF, and larger  $m_{\text{crit}}$  are preferred. However, the difference between maximum likelihood and that of the other models is not so large that it is difficult to distinguish models.

In Figure 19(a)–22(a), the likelihood in the range  $M_t = 600$ – $800$  is not plotted. This is because, as can be seen from Figure 16, BBHs in this mass range do not merge within the horizon of advanced LIGO. When  $\alpha\lambda = 0.1$ , the total mass of BBH mergers with short delay time is  $\sim 250$ – $1500 M_{\odot}$ . On the other hand, BBHs with long delay time have two sub-populations with slightly different formation channels, and total mass is  $\lesssim 600 M_{\odot}$  and  $\gtrsim 800 M_{\odot}$ . Since the horizon of advanced LIGO is  $z \sim 1$  (see Figure 15), only BBHs with long delay time can be observed by advanced LIGO. Therefore, when  $\alpha\lambda = 0.1$ , BBHs with  $M_t = 600$ – $800 M_{\odot}$  cannot be detected by advanced LIGO. On the other hand, since LISA can detect BBHs with short delay time, likelihood ratios are plotted in the range  $M_t = 600$ – $800 M_{\odot}$ .

## 5 SUMMARY

In this paper, we perform a binary population synthesis calculation for very massive ( $\sim 100$ – $1000 M_{\odot}$ ) Pop. III stars and derive the various property of BBH mergers with IMBHs. We adopt wide range of common envelope parameter  $\alpha\lambda$  from 0.01 to 5 and investigate the dependence of  $\alpha\lambda$  on the primary BH mass, mass ratio, effective spin and delay time distribution of BBH mergers. We find that if  $\alpha\lambda$  is smaller, the maximum mass of primary BH mass is larger (Section 3).

We derive the redshift evolution of merger rate density and compare our results with the observation. So far, no BBH with IMBHs have been discovered by gravitational wave detector, and thus only upper limit on merger rate density have been obtained. In this study, we adopt various IMF models and impose restrictions on IMF models by using this upper limit obtained from non-detection (Section 4.1).

We also compute the detection rate by advanced LIGO (O4), Einstein telescope and LISA, and obtain the mass distribution of detected BBHs with IMBHs (Section 4.2.1). We find that Einstein telescope

**Table 8.** Same as Table 7 but for  $\alpha\lambda = 0.1$ .

$\gamma_1$	$m_{\text{crit}} [M_{\odot}]$	$\gamma_2$									
		1.5	2.0	2.5	3.0	3.5	4.0	4.5	5.0		
0.0	100	-	-	0.32 604 <b>76</b>	-	0.10 308 <b>15</b>	0.052 195 <b>5.4</b>	0.033 118 <b>1.5</b>	0.010 71 <b>0.68</b>		
		0.0	200	-	-	-	-	0.20 785 <b>21</b>	0.14 693 <b>13</b>	0.082 587 <b>8.3</b>	
				0.0	300	-	-	-	-	-	0.34 1600 <b>31</b>
1.0	100	-	-			-	0.13 350 <b>25</b>	0.057 222 <b>6.5</b>	0.017 137 <b>0.77</b>	0.012 84 <b>5.1</b>	0.005 47 <b>0.014</b>
		1.0	200	-	-	-	0.30 713 <b>69</b>	0.22 623 <b>28</b>	0.20 543 <b>22</b>	0.13 456 <b>7.5</b>	0.069 378 <b>6.9</b>
				1.0	300	-	-	-	-	-	0.32 1077 <b>39</b>

**Table 9.** Same as Table 7 but for  $\alpha\lambda = 0.5$ .

$\gamma_1$	$m_{\text{crit}} [M_{\odot}]$	$\gamma_2$									
		1.5	2.0	2.5	3.0	3.5	4.0	4.5	5.0		
0.0	100	-	-	-	-	-	-	1.6 212 <b>1.6</b>	0.8 134 <b>0.7</b>	0.5 83 <b>0.4</b>	
		0.0	200	-	-	-	-	-	-	-	-
				0.0	300	-	-	-	-	-	-
1.0	100	-	-			-	-	1.5 240 <b>1.9</b>	1.0 153 <b>0.9</b>	0.6 90 <b>0.5</b>	0.4 56 <b>0.3</b>
		1.0	200	-	-	-	-	-	-	-	
				1.0	300	-	-	-	-	-	-

is a promising detector for the Pop.III BBH mergers with IMBHs, and the detection rate is from  $\sim 10 \text{ yr}^{-1}$  to  $1000 \text{ yr}^{-1}$ .

Finally, we calculate the likelihood ratio for model parameter ( $\alpha\lambda$ ,  $\gamma_1$ ,  $\gamma_2$  and  $m_{\text{crit}}$ ) assuming that one BBH with IMBHs with a certain total mass is observed by certain detector. We find that we can impose restrictions on  $\alpha\lambda$  to some degree if a BBH with total mass  $\gtrsim 500M_{\odot}$  are detected by advanced LIGO (O4) or LISA.

## ACKNOWLEDGEMENTS

This work was supported by JSPS KAKENHI grant No. 17H06360 and 19K03907 (A. T.), 21K13915, 22K03630 (T. K.), 20H05249 (T. Y.), and 17H01130, 17K05380 and 21H01123 (H. U.), and by the University of Tokyo Young Excellent Researcher program (T. K.).

We use the Python packages, numpy (van der Walt et al. 2011) and matplotlib (Hunter 2007) for our analysis.

## DATA AVAILABILITY

Results will be shared on reasonable request to authors.

## REFERENCES

- Abbott R., et al., 2020, *Phys. Rev. Lett.*, **125**, 101102  
Amaro-Seoane P., 2018, *Phys. Rev. D*, **98**, 063018  
Amaro-Seoane P., et al., 2017, arXiv e-prints, p. arXiv:1702.00786  
Anagnostou O., Trenti M., Melatos A., 2020, *Publ. Astron. Soc. Australia*, **37**, e044  
Antonini F., Perets H. B., 2012, *ApJ*, **757**, 27



**Table 10.** Same as Table 7 but for  $\alpha\lambda = 1.0$ .

$\gamma_1$	$m_{\text{crit}} [M_{\odot}]$	$\gamma_2$								
		1.5	2.0	2.5	3.0	3.5	4.0	4.5	5.0	
0.0	100	-	-	-	-	-	-	-	-	0.6 143 <b>0.2</b>
0.0	200	-	-	-	-	-	-	-	-	-
0.0	300	-	-	-	-	-	-	-	-	-
1.0	100	-	-	-	-	-	-	-	0.7 136 <b>0.2</b>	0.5 93 <b>0.1</b>
1.0	200	-	-	-	-	-	-	-	-	-
1.0	300	-	-	-	-	-	-	-	-	-

**Table 11.** Same as Table 7 but for  $\alpha\lambda = 2.0$ .

$\gamma_1$	$m_{\text{crit}} [M_{\odot}]$	$\gamma_2$								
		1.5	2.0	2.5	3.0	3.5	4.0	4.5	5.0	
0.0	100	-	-	-	-	-	-	-	-	0.65 164 <b>0.12</b>
0.0	200	-	-	-	-	-	-	-	-	-
0.0	300	-	-	-	-	-	-	-	-	-
1.0	100	-	-	-	-	-	-	-	0.71 147 <b>0.12</b>	0.41 104 <b>0.02</b>
1.0	200	-	-	-	-	-	-	-	-	-
1.0	300	-	-	-	-	-	-	-	-	-

**Table 12.** Same as Table 7 but for  $\alpha\lambda = 5.0$ .

$\gamma_1$	$m_{\text{crit}} [M_{\odot}]$	$\gamma_2$							
		1.5	2.0	2.5	3.0	3.5	4.0	4.5	5.0
0.0	100	-	-	-	-	-	1.28 216 <b>0.08</b>	0.84 145 <b>0.05</b>	0.53 133 <b>0.03</b>
0.0	200	-	-	-	-	-	-	-	-
0.0	300	-	-	-	-	-	-	-	-
1.0	100	-	-	-	-	-	-	0.56 114 <b>0.03</b>	0.37 85.3 <b>0.02</b>
1.0	200	-	-	-	-	-	-	-	-
1.0	300	-	-	-	-	-	-	-	-

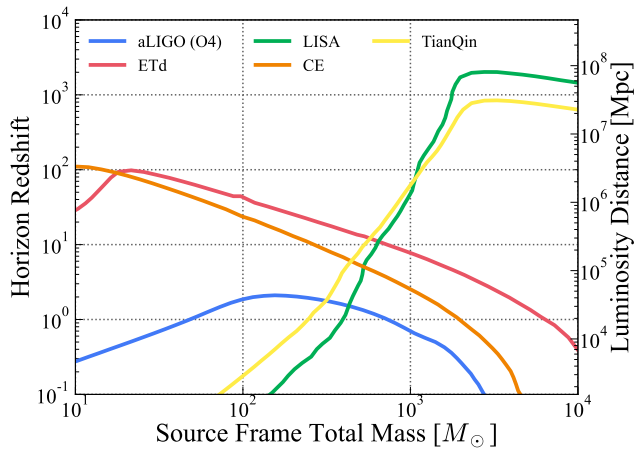


**Figure 15.** The horizon redshift of future GW detectors. The blue, red, green, orange and yellow lines correspond to advanced LIGO (O4), Einstein telescope, LISA, Cosmic Explorer and TianQin respectively.

Antonini F., Rasio F. A., 2016, *ApJ*, **831**, 187  
 Antonini F., Toonen S., Hamers A. S., 2017, *ApJ*, **841**, 77  
 Arca Sedda M., 2020, *ApJ*, **891**, 47  
 Bae Y.-B., Kim C., Lee H. M., 2014, *MNRAS*, **440**, 2714  
 Banerjee S., 2017, *MNRAS*, **467**, 524  
 Banerjee S., 2018a, *MNRAS*, **473**, 909  
 Banerjee S., 2018b, *MNRAS*, **481**, 5123  
 Banerjee S., 2021a, *MNRAS*, **500**, 3002  
 Banerjee S., 2021b, *MNRAS*, **503**, 3371  
 Banerjee S., Baumgardt H., Kroupa P., 2010, *MNRAS*, **402**, 371  
 Bavera S. S., et al., 2021, *A&A*, **647**, A153  
 Belczynski K., 2020, *ApJ*, **905**, L15  
 Belczynski K., et al., 2016, *A&A*, **594**, A97  
 Belczynski K., Ryu T., Perna R., Berti E., Tanaka T. L., Bulik T., 2017, *MNRAS*, **471**, 4702  
 Belczynski K., et al., 2020, *A&A*, **636**, A104  
 Bethe H. A., Brown G. E., 1998, *ApJ*, **506**, 780  
 Di Carlo U. N., Giacobbo N., Mapelli M., Pasquato M., Spera M., Wang L., Haardt F., 2019, *MNRAS*, **487**, 2947  
 Di Carlo U. N., et al., 2020, *MNRAS*, **498**, 495  
 Downing J. M. B., Benacquista M. J., Giersz M., Spurzem R., 2010, *MNRAS*, **407**, 1946  
 Downing J. M. B., Benacquista M. J., Giersz M., Spurzem R., 2011, *MNRAS*, **416**, 133  
 Edwards D. A., Pringle J. E., 1987, *MNRAS*, **229**, 383  
 Eldridge J. J., Stanway E. R., Xiao L., McClelland L. A. S., Taylor G., Ng M., Greis S. M. L., Bray J. C., 2017, *Publ. Astron. Soc. Australia*, **34**, e058  
 Eldridge J. J., Stanway E. R., Tang P. N., 2019, *MNRAS*, **482**, 870  
 Event Horizon Telescope Collaboration et al., 2019a, *ApJ*, **875**, L1  
 Event Horizon Telescope Collaboration et al., 2019b, *ApJ*, **875**, L2  
 Event Horizon Telescope Collaboration et al., 2019c, *ApJ*, **875**, L3  
 Event Horizon Telescope Collaboration et al., 2019d, *ApJ*, **875**, L4  
 Event Horizon Telescope Collaboration et al., 2019e, *ApJ*, **875**, L5  
 Event Horizon Telescope Collaboration et al., 2019f, *ApJ*, **875**, L6  
 Event Horizon Telescope Collaboration et al., 2022a, *ApJ*, **930**, L12  
 Event Horizon Telescope Collaboration et al., 2022b, *ApJ*, **930**, L13  
 Event Horizon Telescope Collaboration et al., 2022c, *ApJ*, **930**, L14  
 Event Horizon Telescope Collaboration et al., 2022d, *ApJ*, **930**, L15  
 Event Horizon Telescope Collaboration et al., 2022e, *ApJ*, **930**, L16  
 Event Horizon Telescope Collaboration et al., 2022f, *ApJ*, **930**, L17  
 Ezquiaga J. M., Holz D. E., 2021, *ApJ*, **909**, L23  
 Farmer R., Renzo M., de Mink S. E., Marchant P., Justham S., 2019, *ApJ*, **887**, 53

Farmer R., Renzo M., de Mink S. E., Fishbach M., Justham S., 2020, *ApJ*, **902**, L36  
 Farr W. M., Fishbach M., Ye J., Holz D. E., 2019, *ApJ*, **883**, L42  
 Farrell S. A., Webb N. A., Barret D., Godet O., Rodrigues J. M., 2009, *Nature*, **460**, 73  
 Farrell E., Groh J. H., Hirschi R., Murphy L., Kaiser E., Ekström S., Georgy C., Meynet G., 2021, *MNRAS*, **502**, L40  
 Fishbach M., Holz D. E., 2020, *ApJ*, **904**, L26  
 Fragione G., Banerjee S., 2021, *ApJ*, **913**, L29  
 Fragione G., Kocsis B., 2019, *MNRAS*, **486**, 4781  
 Fragione G., Loeb A., Rasio F. A., 2020, *ApJ*, **895**, L15  
 Fryer C. L., Belczynski K., Wiktorowicz G., Dominik M., Kalogera V., Holz D. E., 2012, *ApJ*, **749**, 91  
 Fujii M. S., Tanikawa A., Makino J., 2017, *PASJ*, **69**, 94  
 Greene J. E., Strader J., Ho L. C., 2020, *ARA&A*, **58**, 257  
 Hamers A. S., Fragione G., Neunteufel P., Kocsis B., 2021, *MNRAS*, **506**, 5345  
 Hartwig T., Volonteri M., Bromm V., Klessen R. S., Barausse E., Magg M., Stacy A., 2016, *MNRAS*, **460**, L74  
 Hijikawa K., Tanikawa A., Kinugawa T., Yoshida T., Umeda H., 2021, *MNRAS*, **505**, L69  
 Hirano S., Hosokawa T., Yoshida N., Umeda H., Omukai K., Chiaki G., Yorke H. W., 2014, *ApJ*, **781**, 60  
 Hirano S., Hosokawa T., Yoshida N., Omukai K., Yorke H. W., 2015, *MNRAS*, **448**, 568  
 Hong J., Vesperini E., Askar A., Giersz M., Szkudlarek M., Bulik T., 2018, *MNRAS*, **480**, 5645  
 Hong J., Askar A., Giersz M., Hypki A., Yoon S.-J., 2020, *MNRAS*, **498**, 4287  
 Hunter J. D., 2007, *Computing in Science and Engineering*, **9**, 90  
 Hurley J. R., Pols O. R., Tout C. A., 2000, *MNRAS*, **315**, 543  
 Hurley J. R., Tout C. A., Pols O. R., 2002, *MNRAS*, **329**, 897  
 Inayoshi K., Kashiyama K., Visbal E., Haiman Z., 2016, *MNRAS*, **461**, 2722  
 Kinugawa T., Inayoshi K., Hotokezaka K., Nakauchi D., Nakamura T., 2014, *MNRAS*, **442**, 2963  
 Kinugawa T., Miyamoto A., Kanda N., Nakamura T., 2016, *MNRAS*, **456**, 1093  
 Kinugawa T., Nakamura T., Nakano H., 2020, *MNRAS*, **498**, 3946  
 Kinugawa T., Nakamura T., Nakano H., 2021a, *MNRAS*, **501**, L49  
 Kinugawa T., Nakamura T., Nakano H., 2021b, *MNRAS*, **504**, L28  
 Kremer K., et al., 2020, *ApJ*, **903**, 45  
 Kruckow M. U., Tauris T. M., Langer N., Kramer M., Izzard R. G., 2018, *MNRAS*, **481**, 1908  
 Kumamoto J., Fujii M. S., Tanikawa A., 2019, *MNRAS*, **486**, 3942  
 Kumamoto J., Fujii M. S., Tanikawa A., 2020, *MNRAS*, **495**, 4268  
 Kumamoto J., Fujii M. S., Trani A. A., Tanikawa A., 2021, arXiv e-prints, p. arXiv:2102.09323  
 Kuns K. A., Yu H., Chen Y., Adhikari R. X., 2020, *Phys. Rev. D*, **102**, 043001  
 Leigh N. W. C., et al., 2018, *MNRAS*, **474**, 5672  
 Liu B., Bromm V., 2020, *MNRAS*, **495**, 2475  
 Liu B., Bromm V., 2021, *MNRAS*, **506**, 5451  
 Liu B., Meynet G., Bromm V., 2021, *MNRAS*, **501**, 643  
 Luo J., et al., 2016, *Classical and Quantum Gravity*, **33**, 035010  
 Mandel I., de Mink S. E., 2016, *MNRAS*, **458**, 2634  
 Mangiagli A., Bonetti M., Sesana A., Colpi M., 2019, *ApJ*, **883**, L27  
 Mapelli M., 2016, *MNRAS*, **459**, 3432  
 Mapelli M., Giacobbo N., Ripamonti E., Spera M., 2017, *MNRAS*, **472**, 2422  
 Mapelli M., Giacobbo N., Santoliquido F., Artale M. C., 2019, *MNRAS*, **487**, 2  
 Mapelli M., et al., 2021, *MNRAS*, **505**, 339  
 Marchant P., Langer N., Podsiadlowski P., Tauris T. M., Moriya T. J., 2016, *A&A*, **588**, A50  
 Matsubayashi T., Shinkai H.-a., Ebisuzaki T., 2004, *ApJ*, **614**, 864  
 McKernan B., et al., 2018, *ApJ*, **866**, 66  
 Nitz A. H., Capano C. D., 2021, *ApJ*, **907**, L9  
 O’Leary R. M., Rasio F. A., Fregeau J. M., Ivanova N., O’Shaughnessy R., 2006, *ApJ*, **637**, 937  
 O’Leary R. M., Kocsis B., Loeb A., 2009, *MNRAS*, **395**, 2127

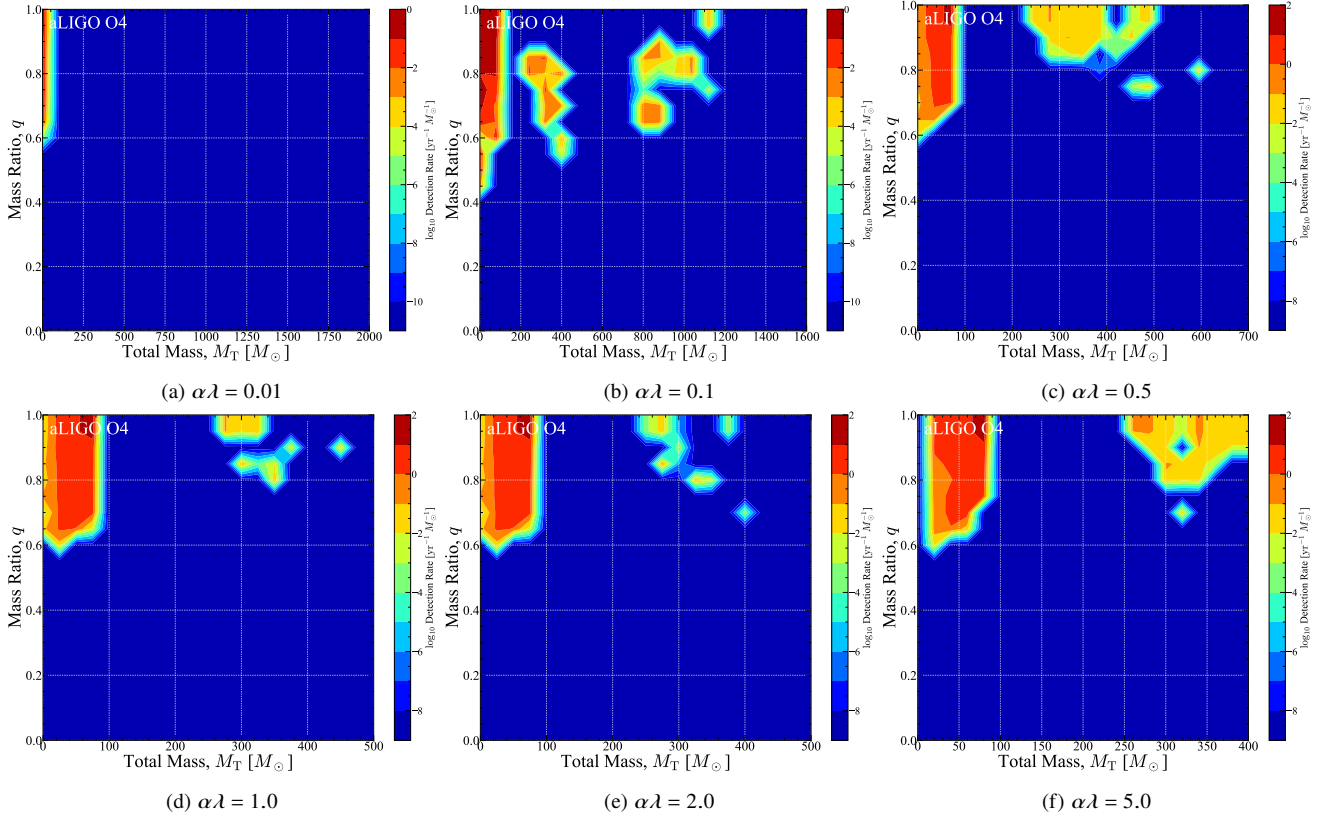


**Figure 16.** The detection rate by advanced LIGO for each  $\alpha\lambda$ . Note that not all panels have the same color scale.

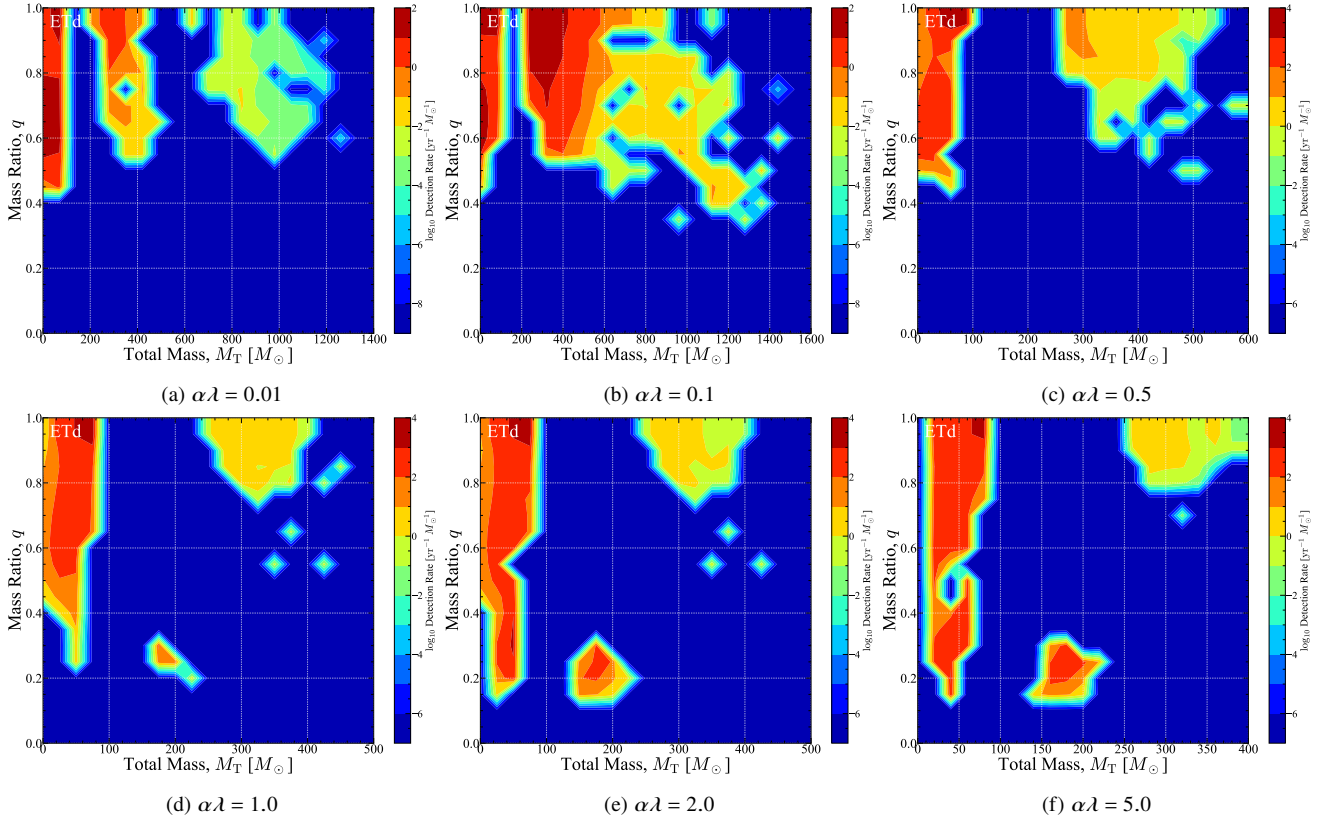


**Figure 17.** The detection rate by Einstein telescope for each  $\alpha\lambda$ . Note that not all panels have the same color scale.

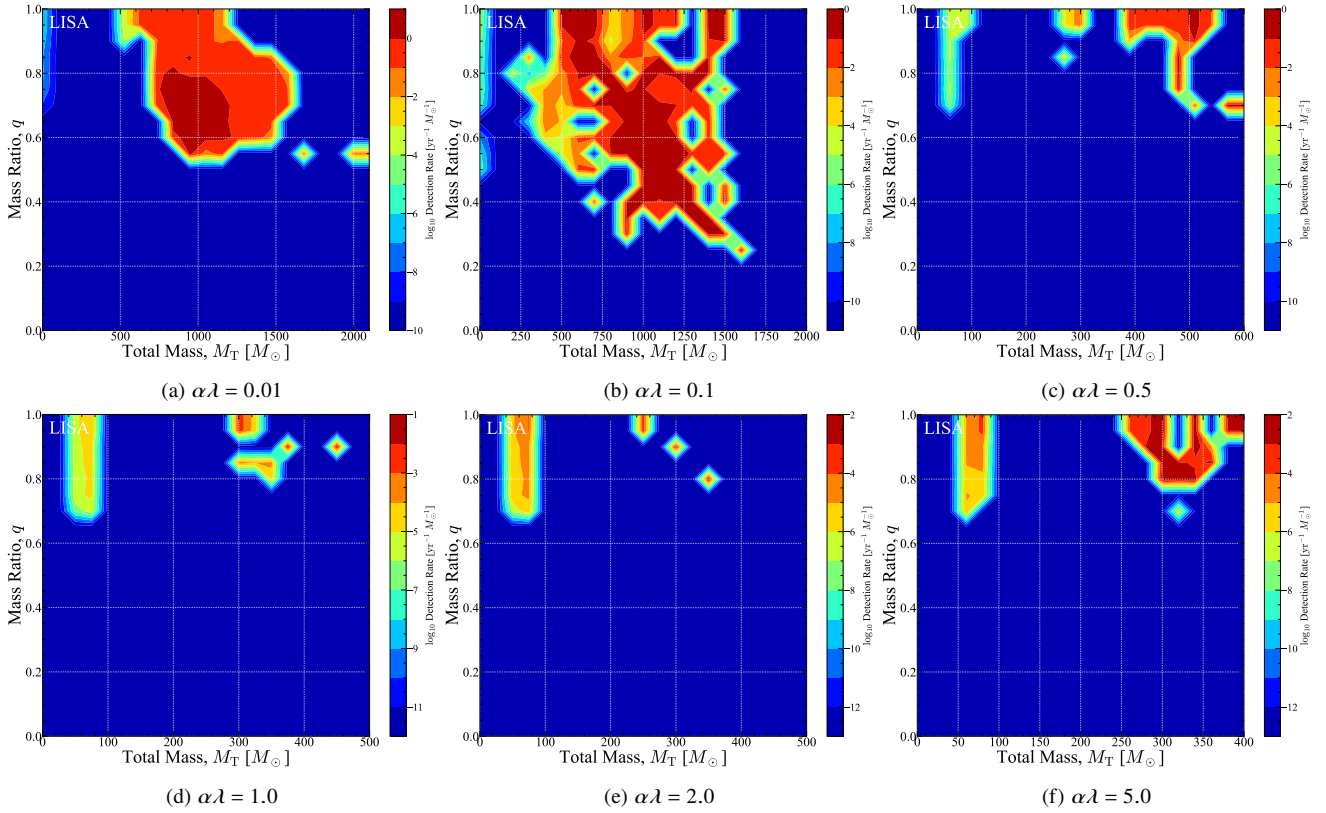


**Figure 18.** The detection rate by LISA for each  $\alpha\lambda$ . Note that not all panels have the same color scale.

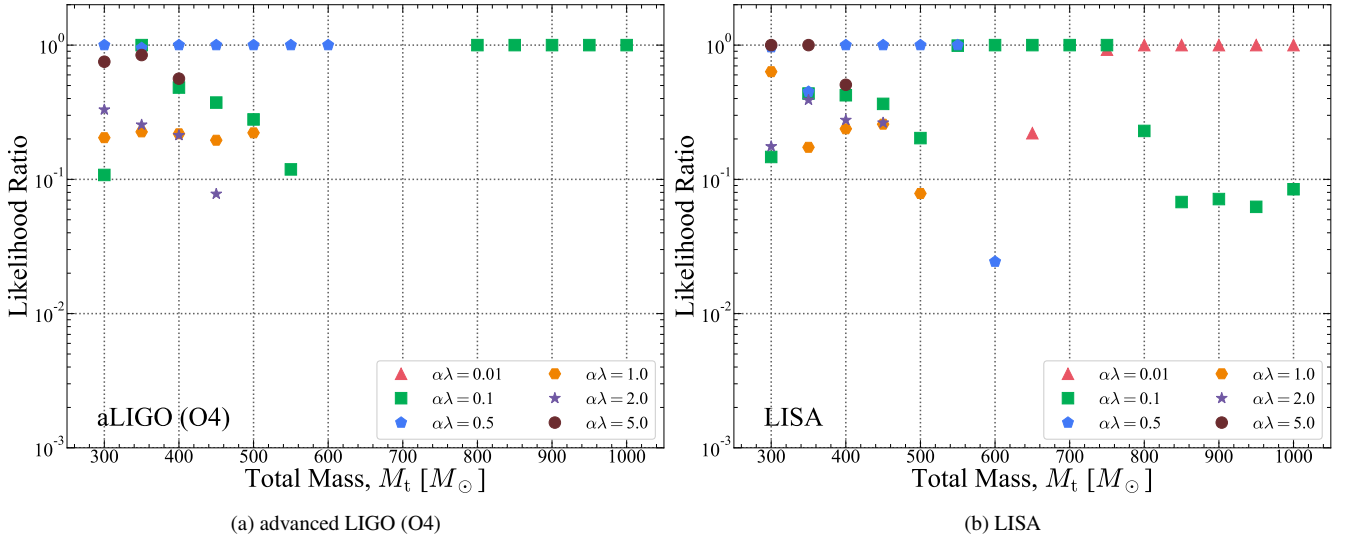


**Figure 19.** The likelihood ratio of  $\alpha\lambda$  for each detector.

Paczynski B., Sienkiewicz R., 1972, *Acta Astron.*, **22**, 73  
 Park D., Kim C., Lee H. M., Bae Y.-B., Belczynski K., 2017, *MNRAS*, **469**, 4665  
 Pavlovskii K., Ivanova N., Belczynski K., Van K. X., 2017, *MNRAS*, **465**, 2092  
 Planck Collaboration et al., 2020, *A&A*, **641**, A6  
 Portegies Zwart S. F., McMillan S. L. W., 2000, *ApJ*, **528**, L17  
 Punturo M., et al., 2010, *Classical and Quantum Gravity*, **27**, 194002  
 Qin Y., Fragos T., Meynet G., Andrews J., Sørensen M., Song H. F., 2018, *A&A*, **616**, A28

Rasskazov A., Kocsis B., 2019, *ApJ*, **881**, 20  
 Reitze D., et al., 2019, in *Bulletin of the American Astronomical Society*, p. 35 ([arXiv:1907.04833](https://arxiv.org/abs/1907.04833))  
 Riley J., Mandel I., Marchant P., Butler E., Nathaniel K., Neijssel C., Shortt S., Vigna-Gómez A., 2021, *MNRAS*, **505**, 663  
 Rodriguez C. L., Antonini F., 2018, *ApJ*, **863**, 7  
 Rodriguez C. L., Chatterjee S., Rasio F. A., 2016, *Phys. Rev. D*, **93**, 084029  
 Rodriguez C. L., Amaro-Seoane P., Chatterjee S., Rasio F. A., 2018, *Phys. Rev. Lett.*, **120**, 151101  
 Rodriguez C. L., Zevin M., Amaro-Seoane P., Chatterjee S., Kremer K., Rasio



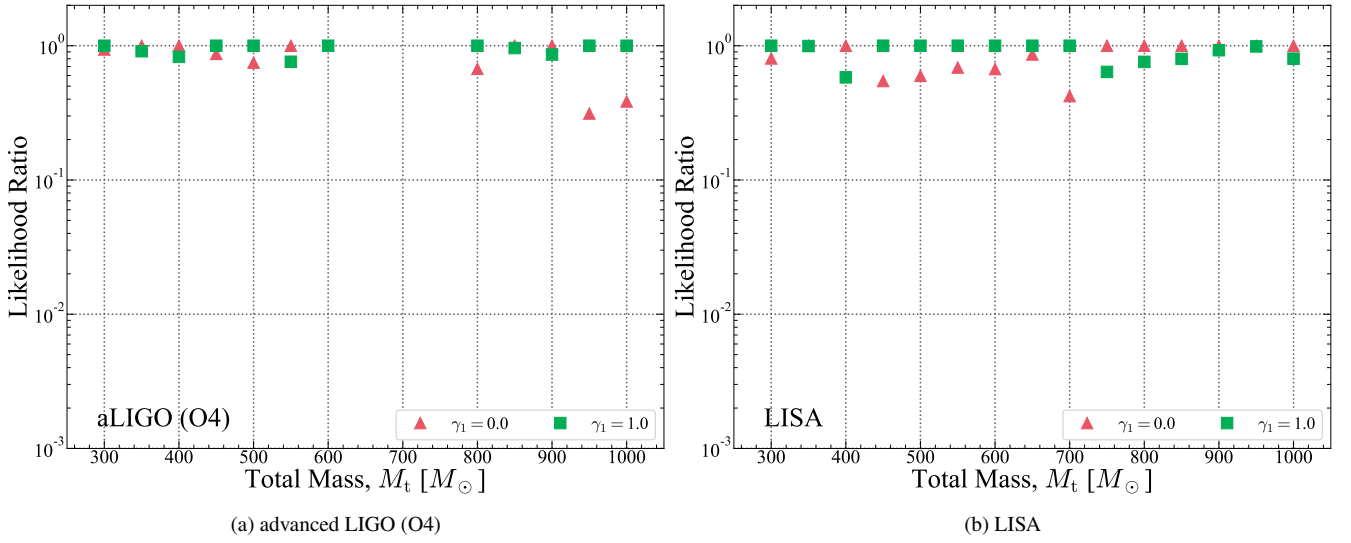


Figure 20. The likelihood ratio of  $\gamma_1$  for each detector.

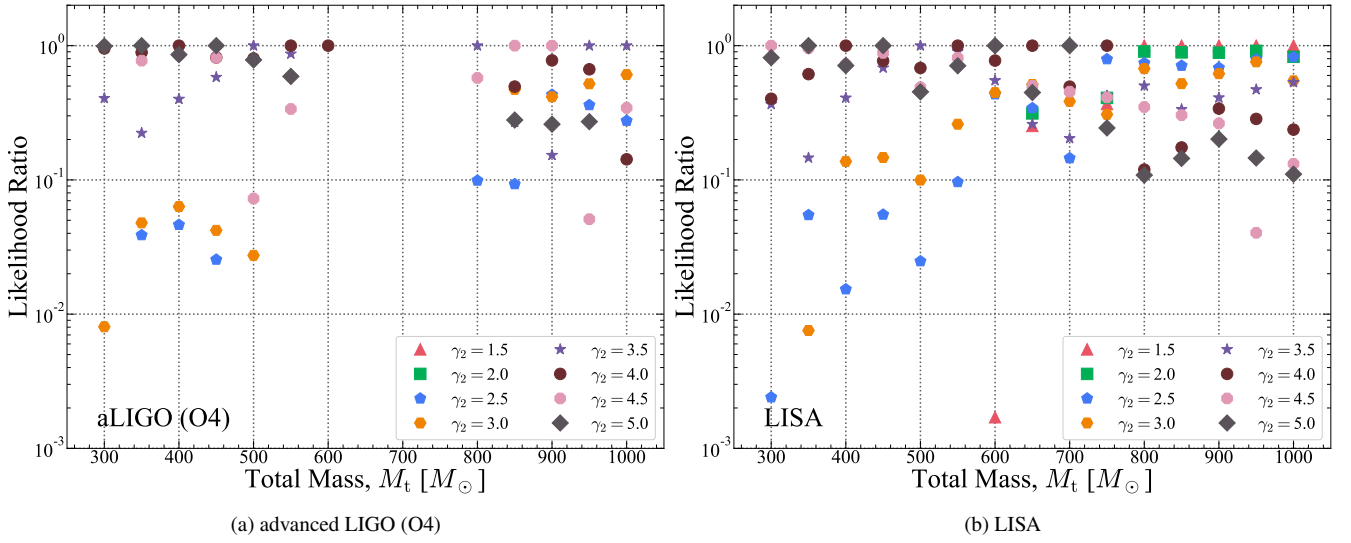
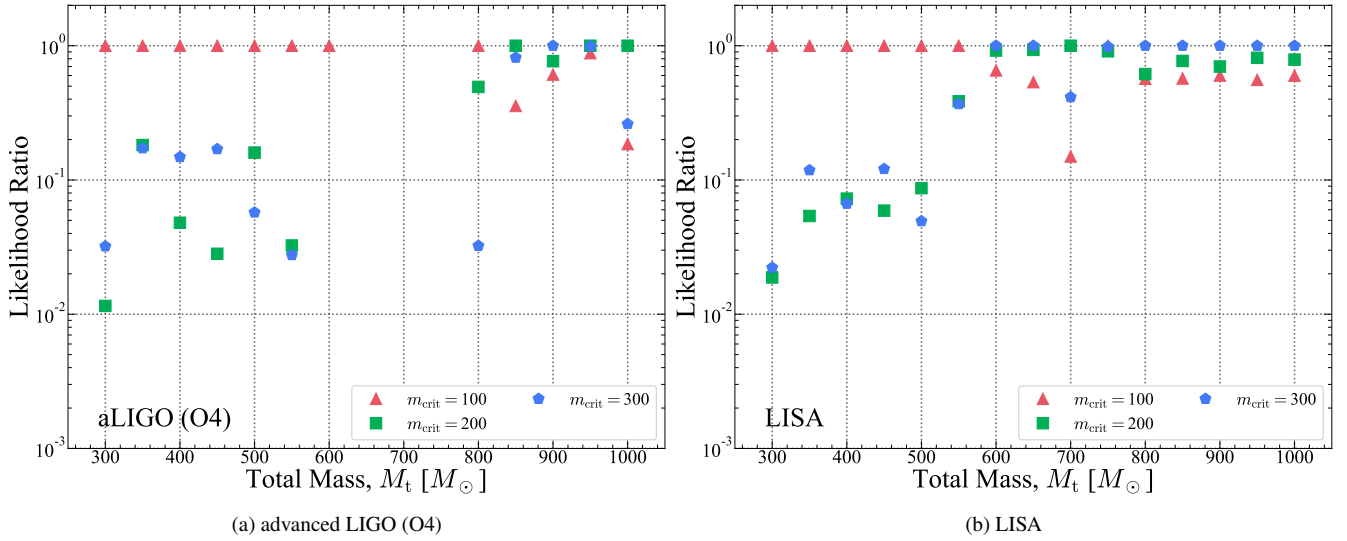


Figure 21. The likelihood ratio of  $\gamma_2$  for each detector.

F. A., Ye C. S., 2019, *Phys. Rev. D*, **100**, 043027  
 Sadowski A., Belczynski K., Bulik T., Ivanova N., Rasio F. A., O’Shaughnessy R., 2008, *ApJ*, **676**, 1162  
 Samsing J., 2018, *Phys. Rev. D*, **97**, 103014  
 Samsing J., Askar A., Giersz M., 2018, *ApJ*, **855**, 124  
 Sathyaprakash B., et al., 2012, *Classical and Quantum Gravity*, **29**, 124013  
 Savonije G. J., 1978, *A&A*, **62**, 317  
 Seto N., Kawamura S., Nakamura T., 2001, *Phys. Rev. Lett.*, **87**, 221103  
 Shinkai H.-a., Kanda N., Ebisuzaki T., 2017, *ApJ*, **835**, 276  
 Silsbee K., Tremaine S., 2017, *ApJ*, **836**, 39  
 Sopuerta C. F., Yunes N., 2009, *Phys. Rev. D*, **80**, 064006  
 Stevenson S., Vigna-Gómez A., Mandel I., Barrett J. W., Neijssel C. J., Perkins D., de Mink S. E., 2017, *Nature Communications*, **8**, 14906  
 Stone N. C., Metzger B. D., Haiman Z., 2017, *MNRAS*, **464**, 946  
 Susa H., Hasegawa K., Tominaga N., 2014, *ApJ*, **792**, 32  
 Tagawa H., Haiman Z., Kocsis B., 2020a, *ApJ*, **898**, 25  
 Tagawa H., Haiman Z., Bartos I., Kocsis B., 2020b, *ApJ*, **899**, 26  
 Tagawa H., Kocsis B., Haiman Z., Bartos I., Omukai K., Samsing J., 2021a, *ApJ*, **907**, L20  
 Tagawa H., Kocsis B., Haiman Z., Bartos I., Omukai K., Samsing J., 2021b, *ApJ*, **908**, 194

Takahashi K., Yoshida T., Umeda H., Sumiyoshi K., Yamada S., 2016, *MNRAS*, **456**, 1320  
 Takahashi K., Yoshida T., Umeda H., 2018, *ApJ*, **857**, 111  
 Takahashi K., Sumiyoshi K., Yamada S., Umeda H., Yoshida T., 2019, *ApJ*, **871**, 153  
 Tanikawa A., 2013, *MNRAS*, **435**, 1358  
 Tanikawa A., Yoshida T., Kinugawa T., Takahashi K., Umeda H., 2020, *MNRAS*, **495**, 4170  
 Tanikawa A., Kinugawa T., Yoshida T., Hijikawa K., Umeda H., 2021a, *MNRAS*, **505**, 2170  
 Tanikawa A., Susa H., Yoshida T., Trani A. A., Kinugawa T., 2021b, *ApJ*, **910**, 30  
 Tanikawa A., Yoshida T., Kinugawa T., Trani A. A., Hosokawa T., Susa H., Omukai K., 2022, *ApJ*, **926**, 83  
 The LIGO Scientific Collaboration the Virgo Collaboration the KAGRA Collaboration 2021a, arXiv e-prints, p. [arXiv:2105.15120](https://arxiv.org/abs/2105.15120)  
 The LIGO Scientific Collaboration et al., 2021b, arXiv e-prints, p. [arXiv:2111.03606](https://arxiv.org/abs/2111.03606)  
 Trani A. A., Tanikawa A., Fujii M. S., Leigh N. W. C., Kumamoto J., 2021, *MNRAS*, **504**, 910  
 Trani A. A., Rastello S., Di Carlo U. N., Santoliquido F., Tanikawa A., Mapelli



**Figure 22.** The likelihood ratio of  $m_{\text{crit}}$  for each detector.

- M., 2022, *MNRAS*, **511**, 1362
- Umeda H., Yoshida T., Nagele C., Takahashi K., 2020, *ApJ*, **905**, L21
- Vink J. S., Higgins E. R., Sander A. A. C., Sabhahit G. N., 2021, *MNRAS*, **504**, 146
- Vynatheya P., Hamers A. S., 2022, *ApJ*, **926**, 195
- Wang H.-T., et al., 2019, *Phys. Rev. D*, **100**, 043003
- Wang L., Tanikawa A., Fujii M., 2022, *MNRAS*, **515**, 5106
- Weatherford N. C., Fragione G., Kremer K., Chatterjee S., Ye C. S., Rodriguez C. L., Rasio F. A., 2021, *ApJ*, **907**, L25
- Webbink R. F., 1984, *ApJ*, **277**, 355
- Yang Y., Bartos I., Haiman Z., Kocsis B., Márka Z., Stone N. C., Márka S., 2019, *ApJ*, **876**, 122
- Yoshida T., Takiwaki T., Kotake K., Takahashi K., Nakamura K., Umeda H., 2019, *ApJ*, **881**, 16
- Ziosi B. M., Mapelli M., Branchesi M., Tormen G., 2014, *MNRAS*, **441**, 3703
- de Souza R. S., Yoshida N., Ioka K., 2011, *A&A*, **533**, A32
- van der Walt S., Colbert S. C., Varoquaux G., 2011, *Computing in Science and Engineering*, **13**, 22

This paper has been typeset from a  $\text{\TeX}/\text{\LaTeX}$  file prepared by the author.